Electronic Supporting Information for

Physical Properties, Ligand Substitution Reactions, and Biological Activity of Co(III)-Schiff Base Complexes

A. Paden King, Hendryck A. Gellineau, Samantha N. MacMillan, and Justin J. Wilson*

Department of Chemistry and Chemical Biology, Cornell University, Ithaca, NY 14853

*e-mail: jjw275@cornell.edu

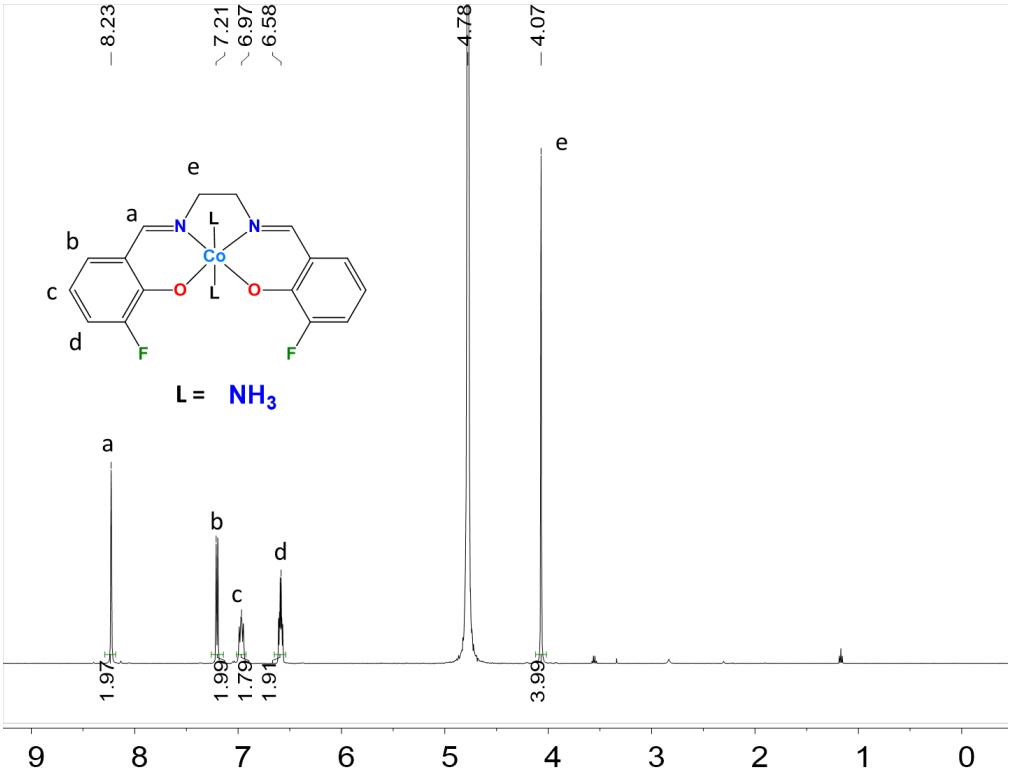

Figure S1. ^{1}H NMR (500 MHz) spectrum of $[Co(3F\text{-}salen)(NH_3)_2]^+$ in MeOD-d_4 at 298 K.

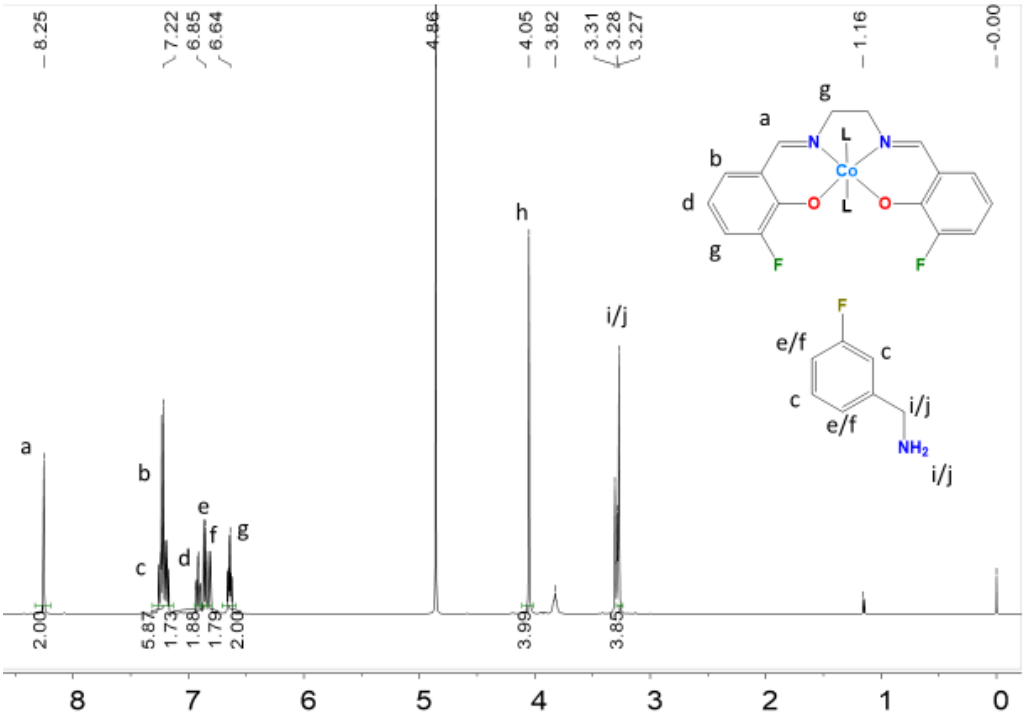

Figure S2. ^{1}H NMR (500 MHz) spectrum of $[Co(3F\text{-}salen)(3F\text{-}BnNH_2)_2]^+$ in MeOD-d_4 at 298 K.

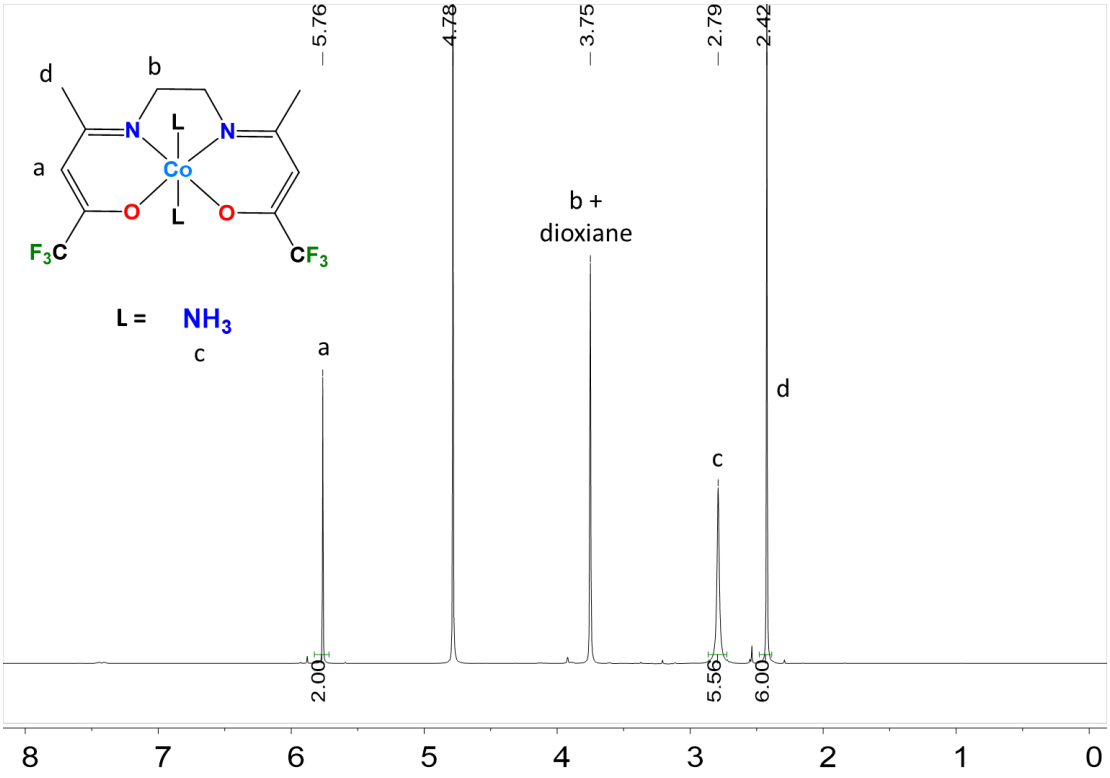

Figure S3. ^{1}H NMR (500 MHz) spectrum of $[Co(tfacen)(NH_3)_2]^+$ in D_2O at 298 K.

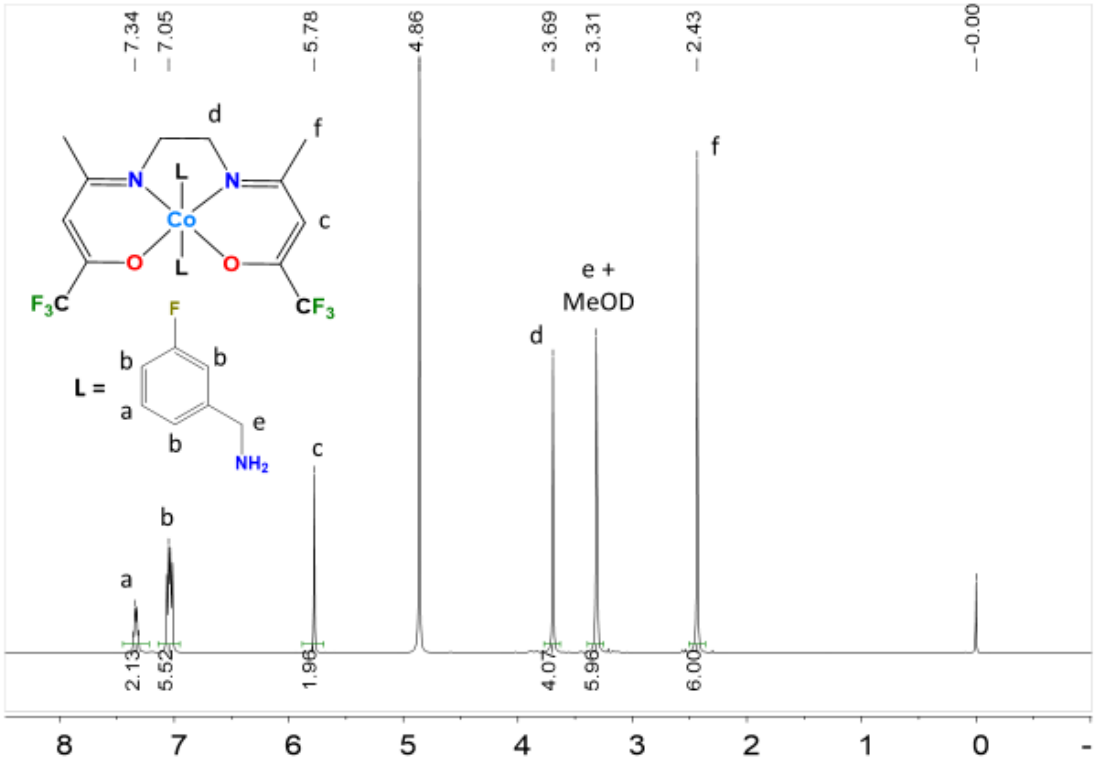

Figure S4. ^{1}H NMR (500 MHz) spectrum of $[Co(tfacen)(3F\text{-}BnNH_2)_2]^+$ in MeOD-d_4 at 298 K.

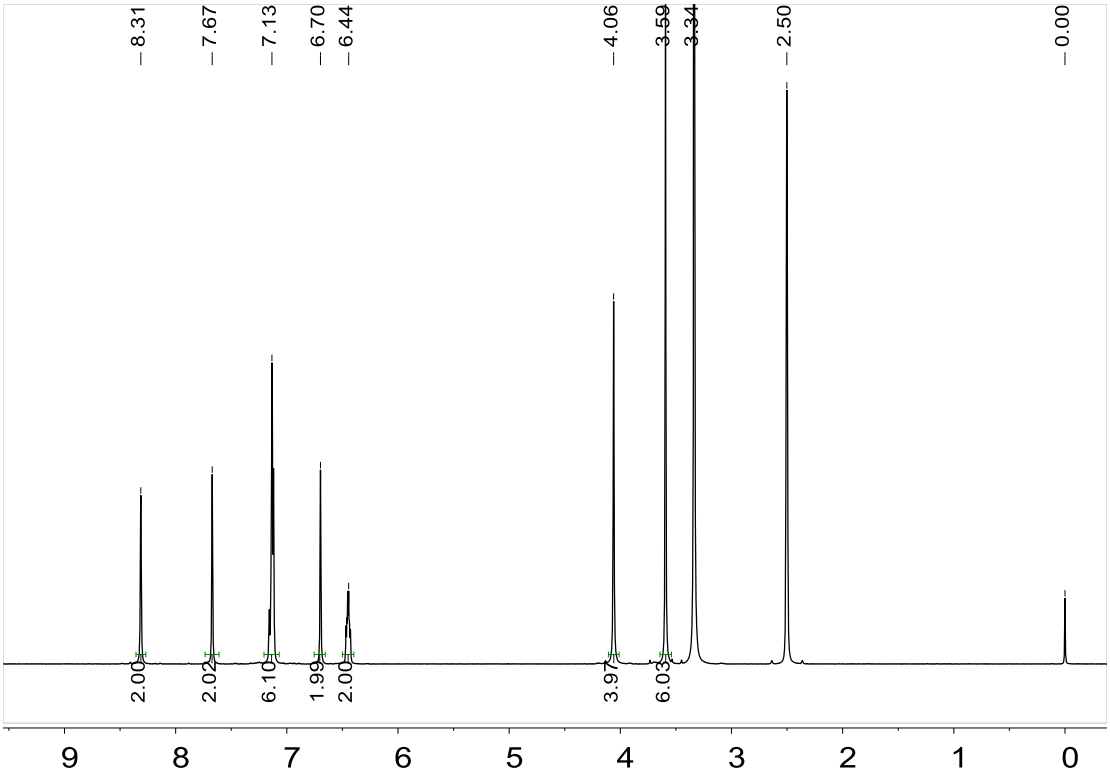

Figure S5. ^{1}H NMR (500 MHz) spectrum of $[Co(3F\text{-}salen)(MeIm)_2]^+$ in DMSO-d_6 at 298 K.

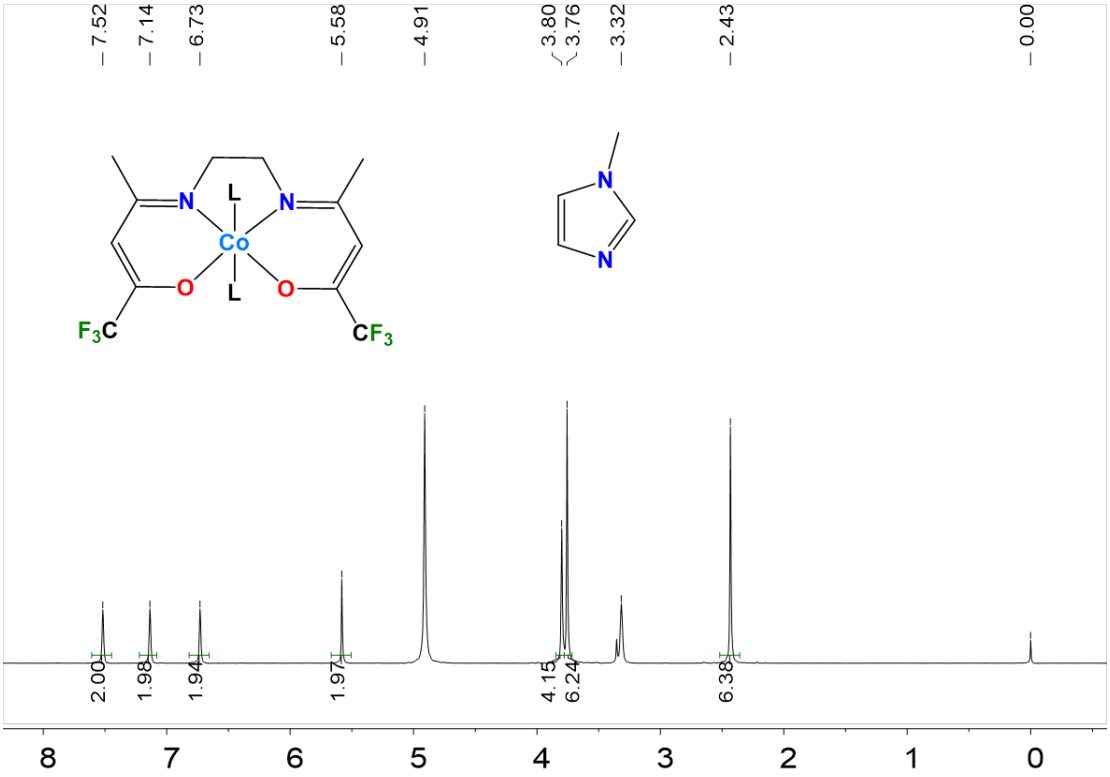

Figure S6. ^{1}H NMR (500 MHz) spectrum of $[Co(tfacen)(MeIm)_2]^+$ in MeOD-d_4 at 298 K.

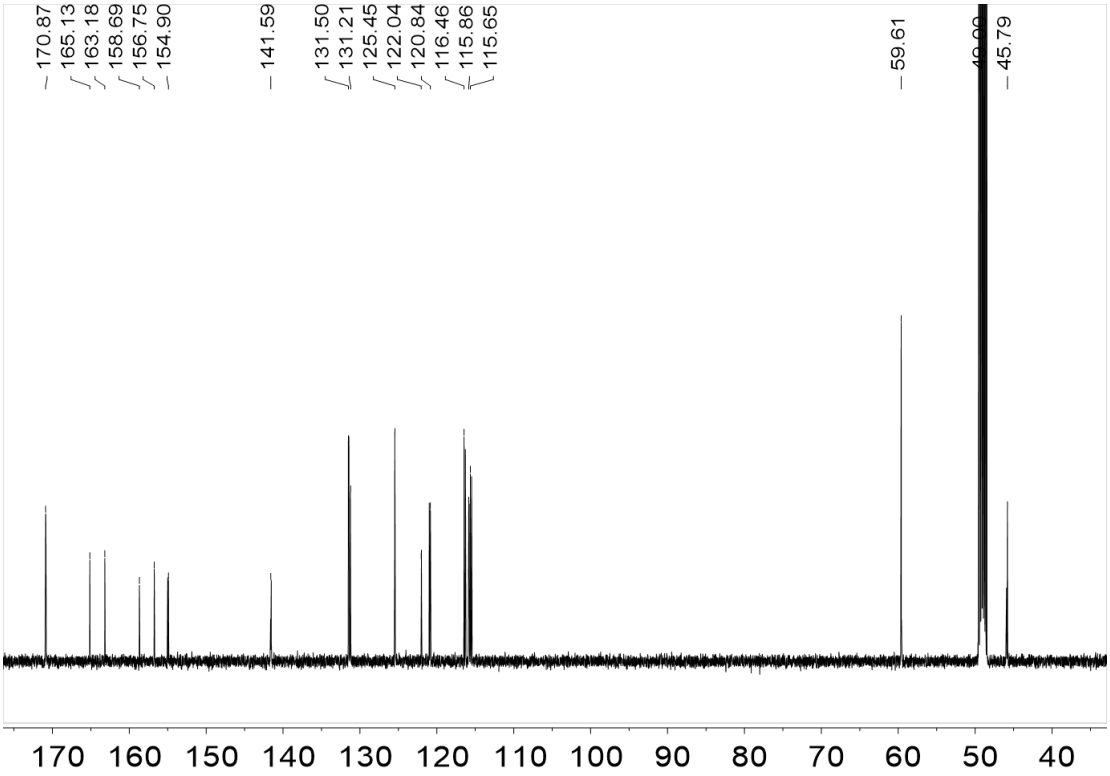

Figure S7. $^{13}C\{^{1}H\}$ NMR (126 MHz) spectrum of $[Co(3F\text{-}salen)(3F\text{-}BnNH_2)_2]^+$ in MeOD-d_4 at 298 K.

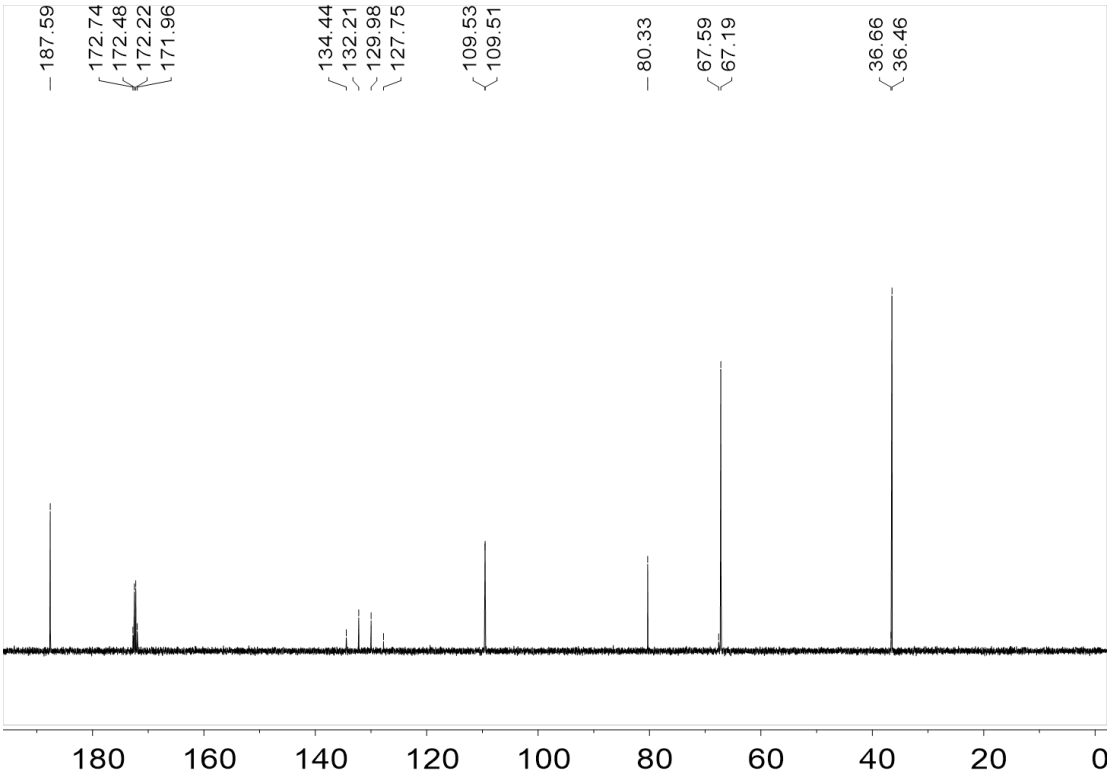

Figure S8. $^{13}C\{^{1}H\}$ NMR (126 MHz) spectrum of $[Co(tfacen)(NH_3)_2]^+$ in D_2O at 298 K.

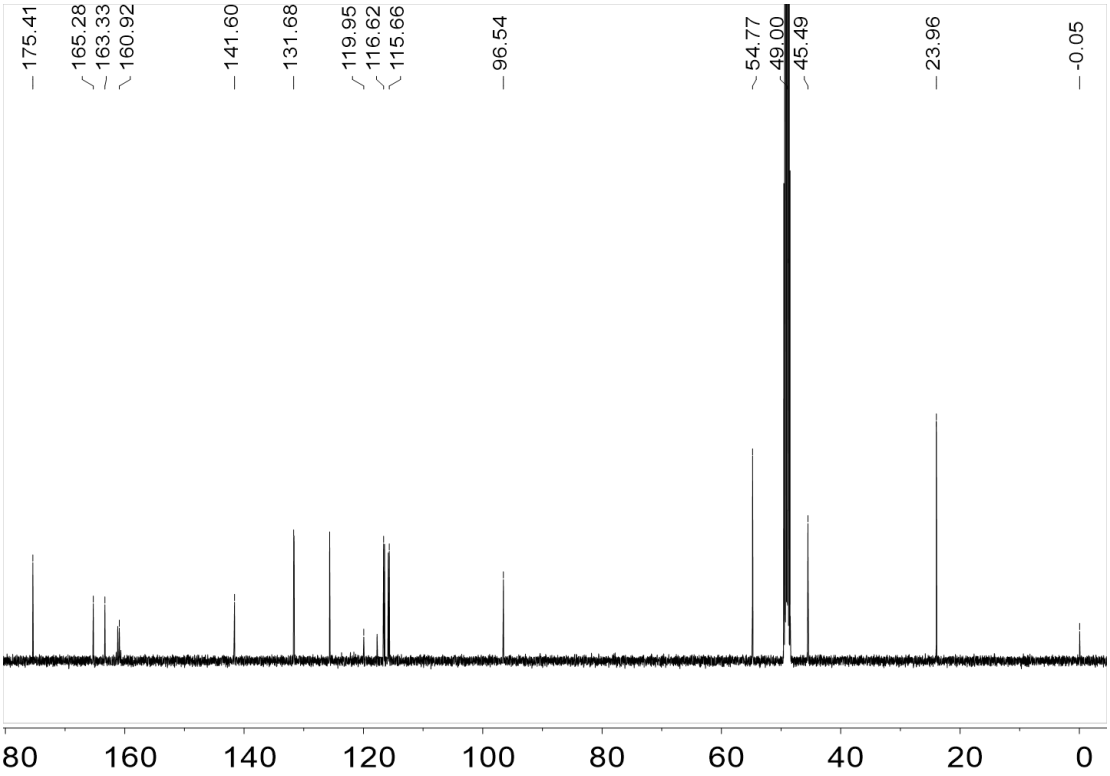

Figure S9. $^{13}C\{^{1}H\}$ NMR (126 MHz) spectrum of $[Co(tfacen)(3F\text{-}BnNH_2)_2]^+$ in MeOD-d_4 at 298 K.

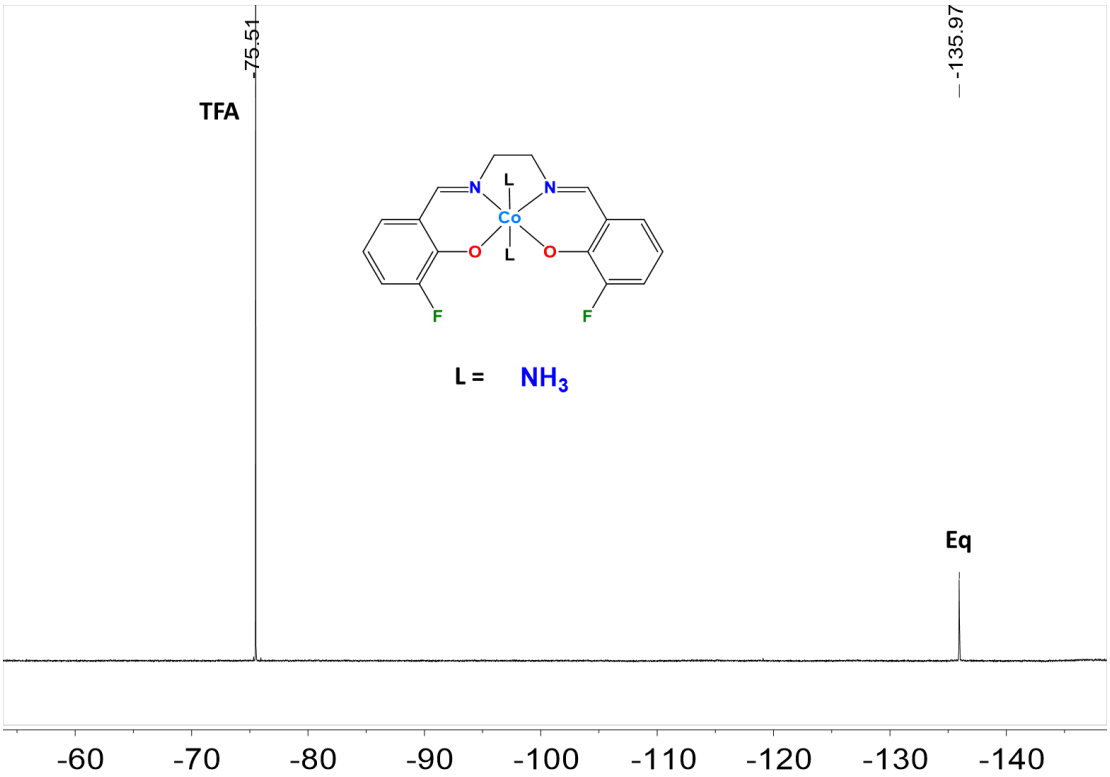

Figure S10. ^{19}F NMR (470 MHz) spectrum of $[Co(3F\text{-}salen)(NH_3)_2]^+$ in H_2O at 298 K.

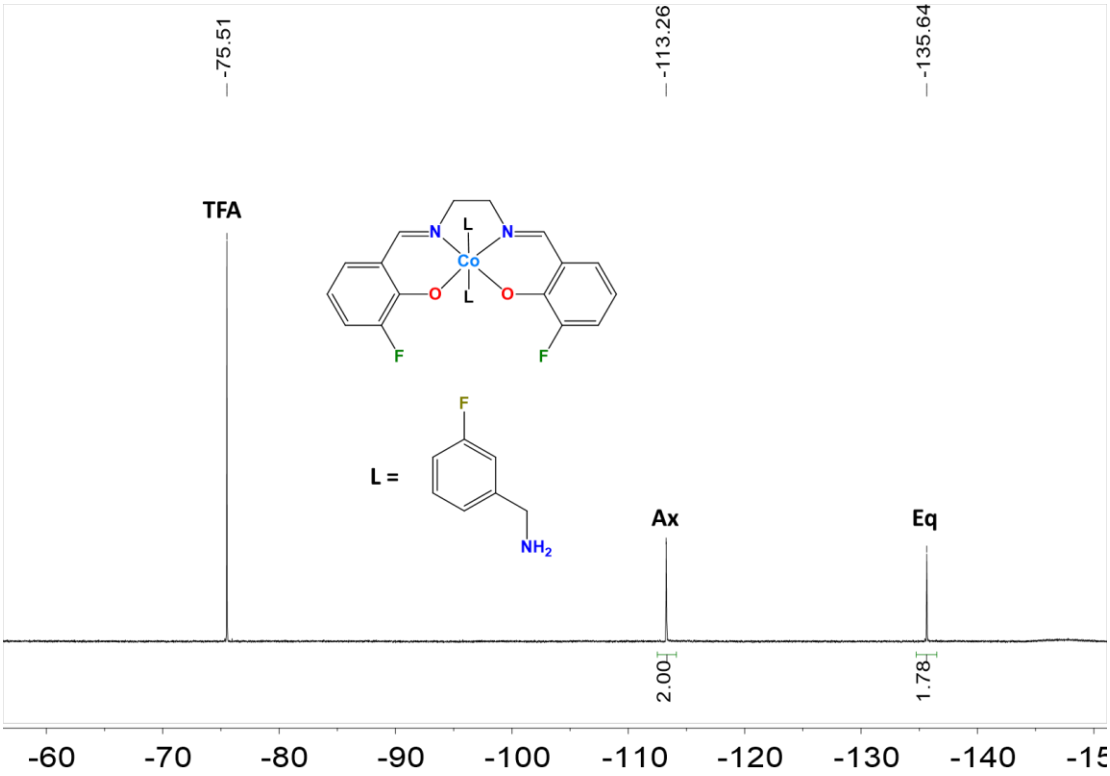

Figure S11. ^{19}F NMR (470 MHz) spectrum of $[Co(3F\text{-}salen)(3F\text{-}BnNH_2)_2]^+$ in H_2O at 298 K.

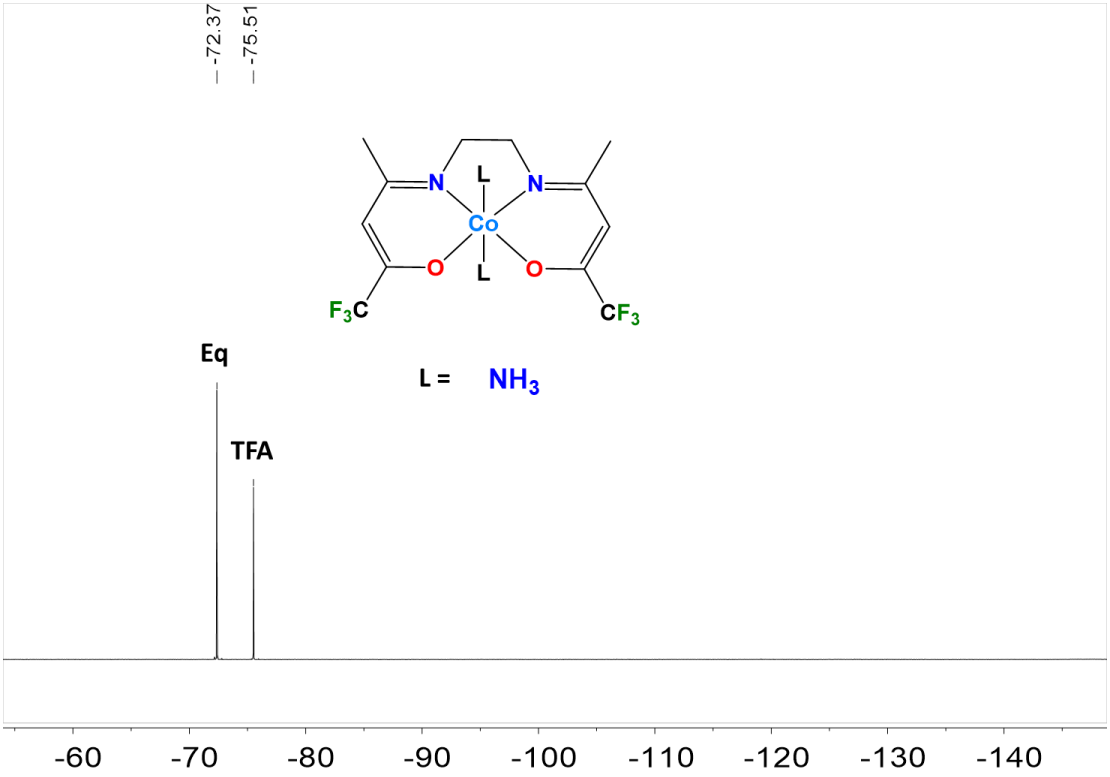

Figure S12. ^{19}F NMR (470 MHz) spectrum of $[Co(tfacen)(NH_3)_2]^+$ in H_2O at 298 K.

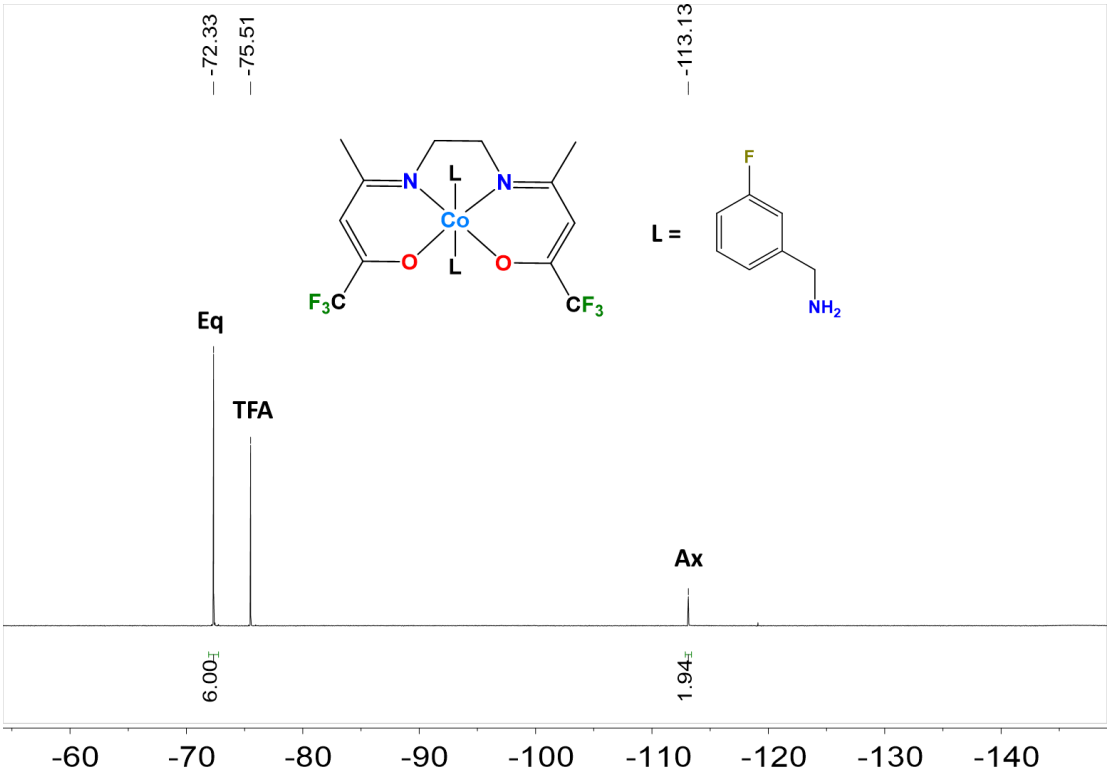

Figure S13. ^{19}F NMR (470 MHz) spectrum of $[Co(tfacen)(3F\text{-}BnNH_2)_2]^+$ in H_2O at 298 K.

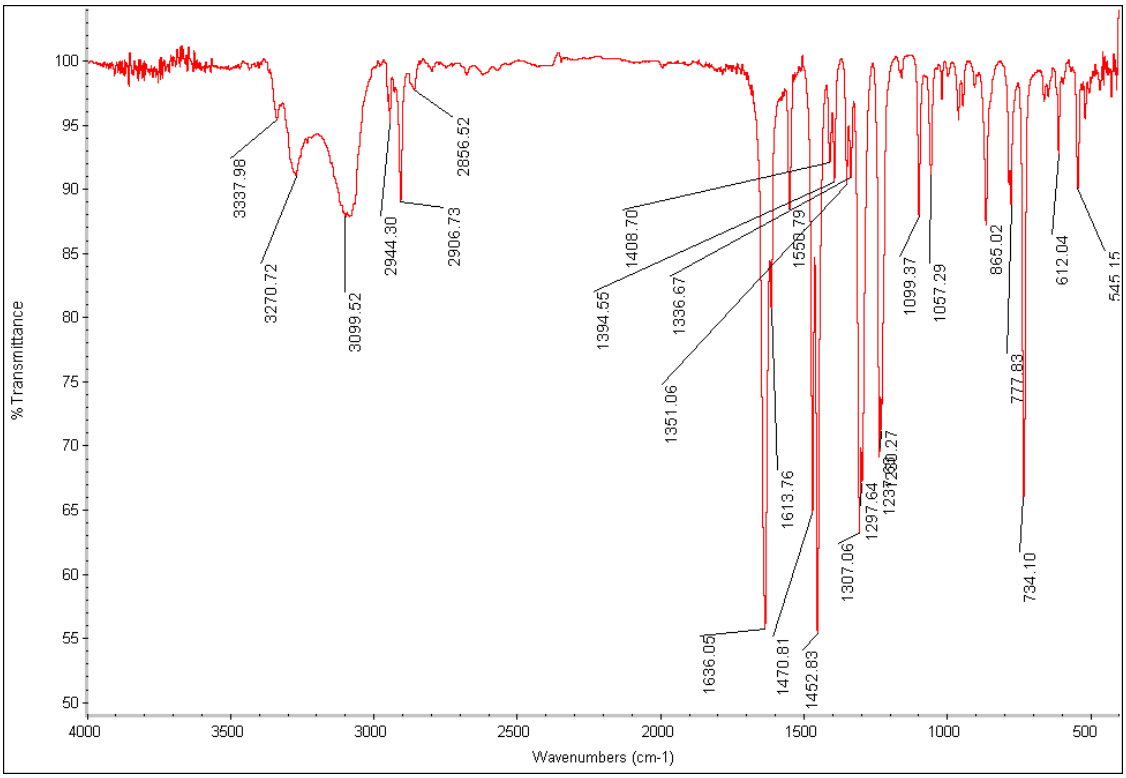

Figure S14. IR spectrum of $[Co(3F\text{-}salen)(NH_3)_2]^+$

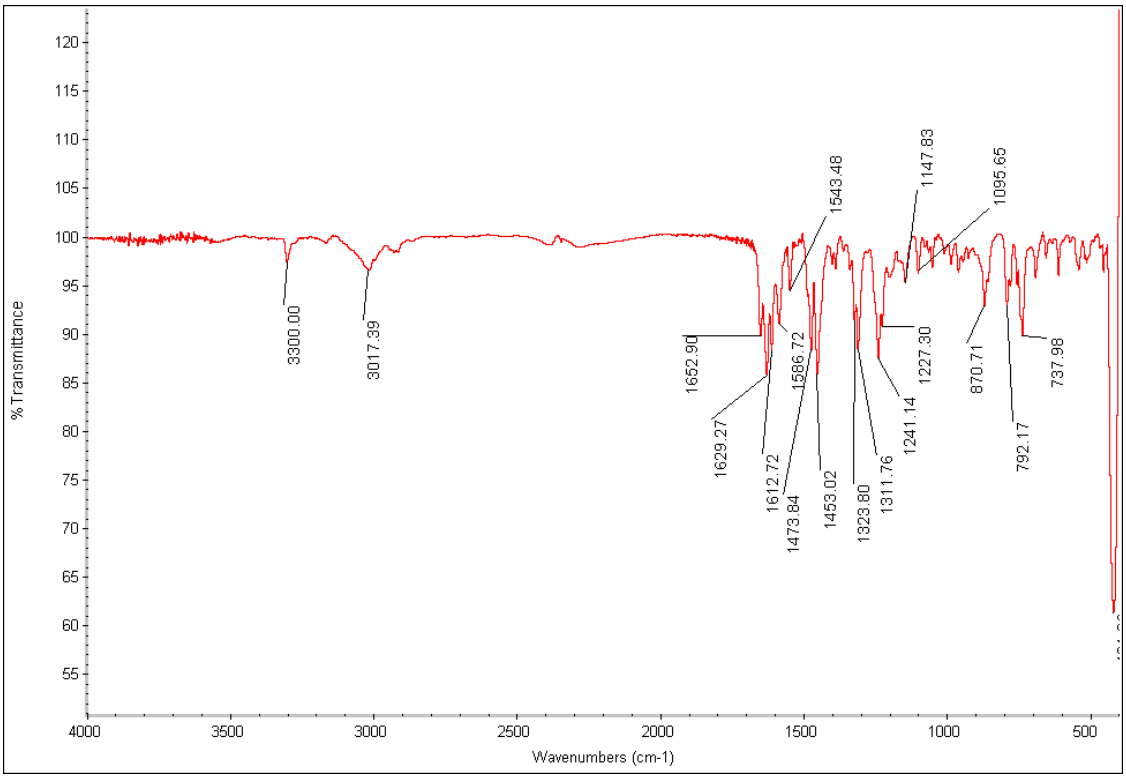

Figure S15. IR spectrum of $[Co(3F\text{-}salen)(3F\text{-}BnNH_2)_2]^+$

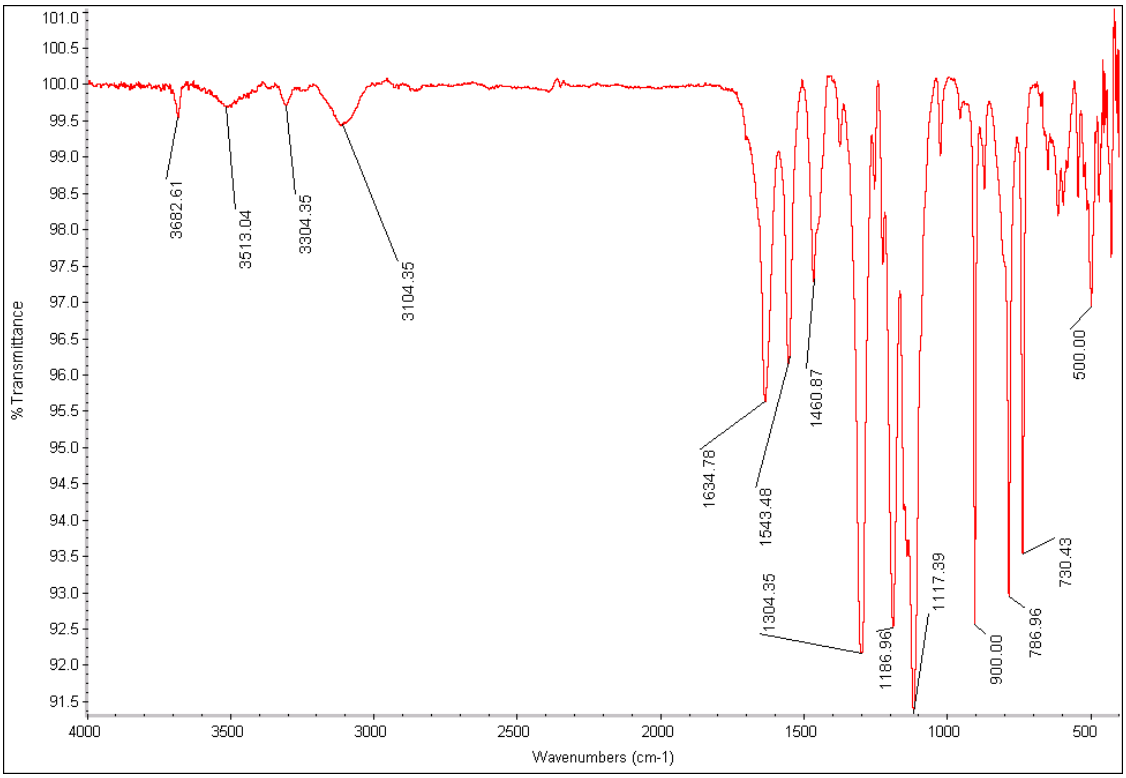

Figure S16. IR spectrum of $[Co(tfacen)(NH_3)_2]^+$

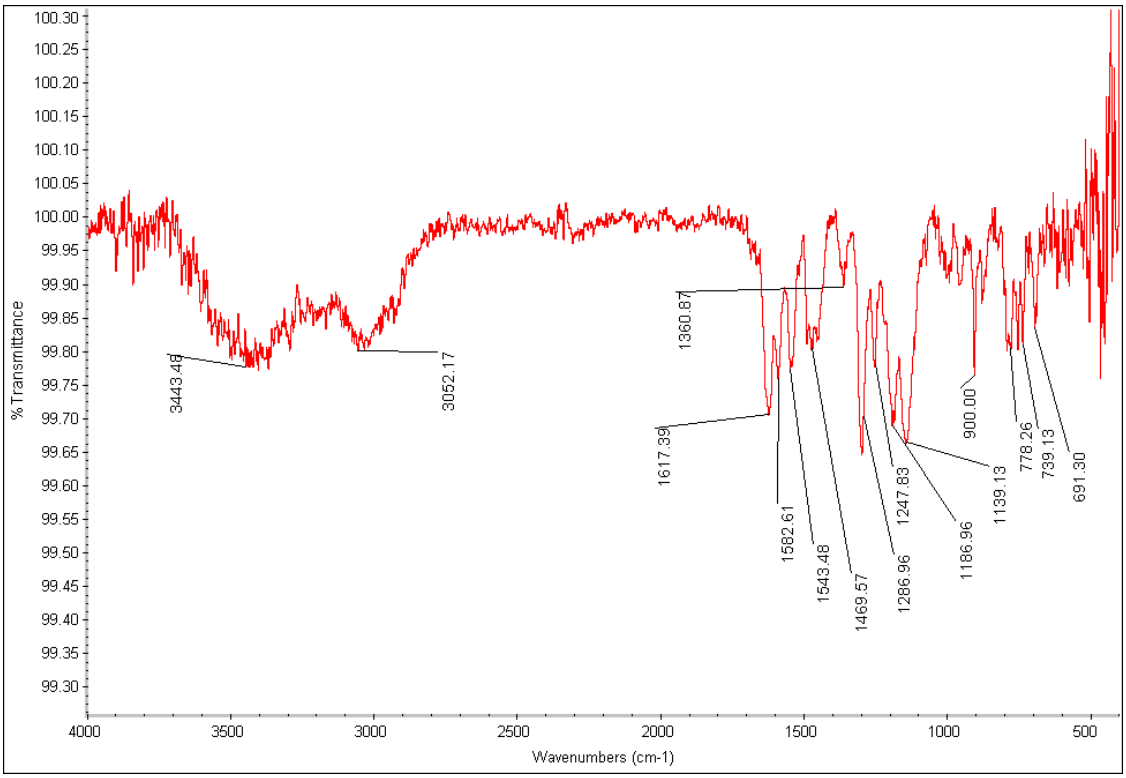

Figure S17. IR spectrum of $[Co(tfacen)(3F\text{-}BnNH_2)_2]^+$

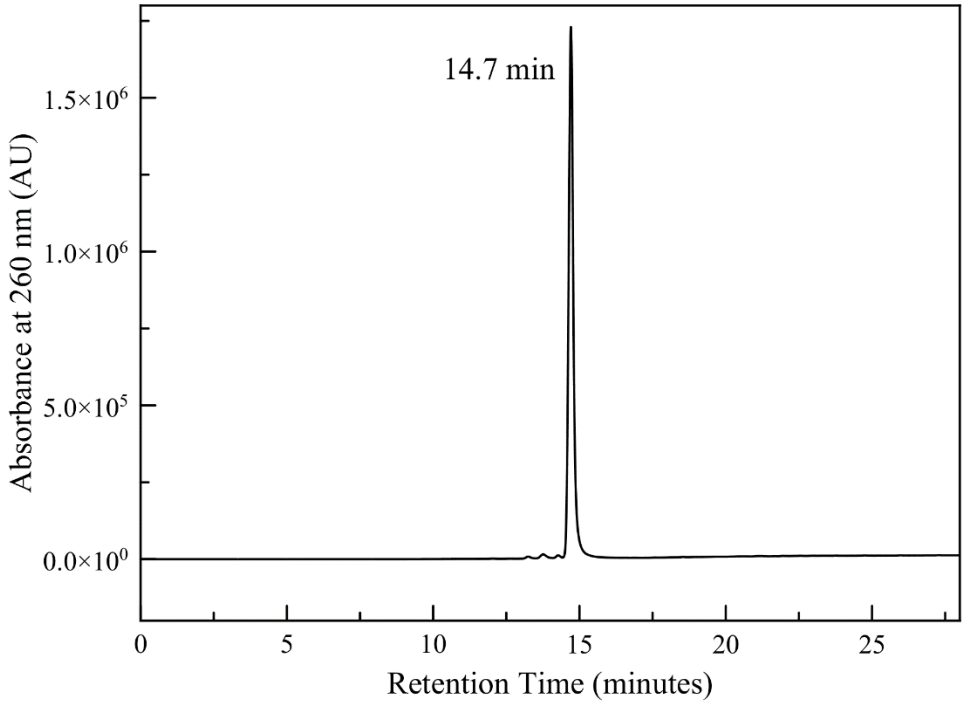

Figure S18. HPLC chromatogram of $[Co(3F\text{-}salen)(NH_3)_2]^+$

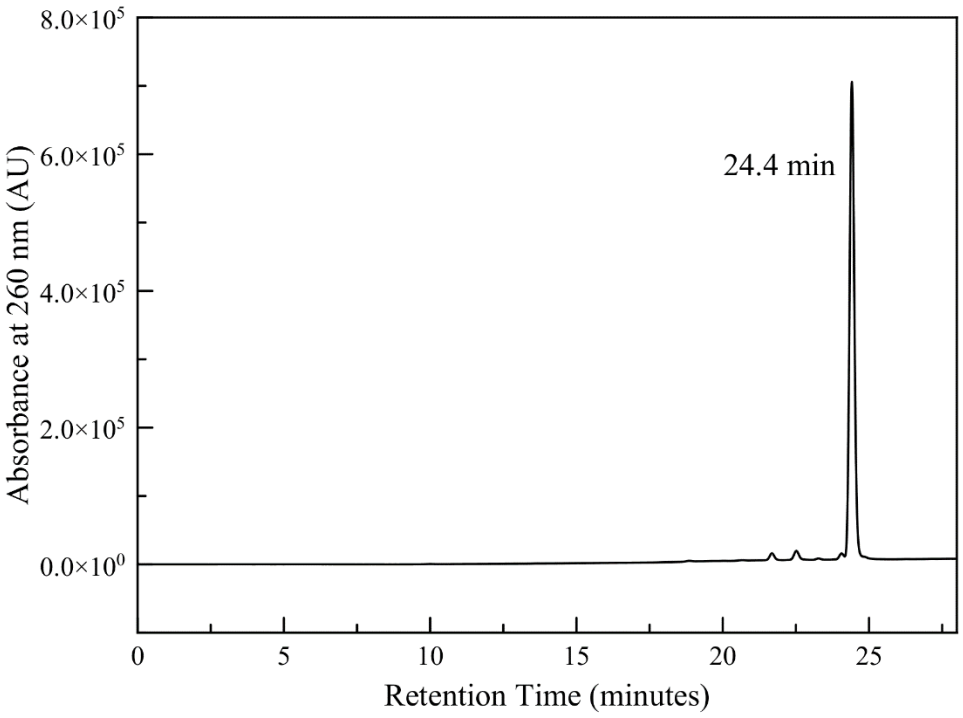

Figure S19. HPLC chromatogram of $[Co(3F\text{-}salen)(3F\text{-}BnNH_2)_2]^+$

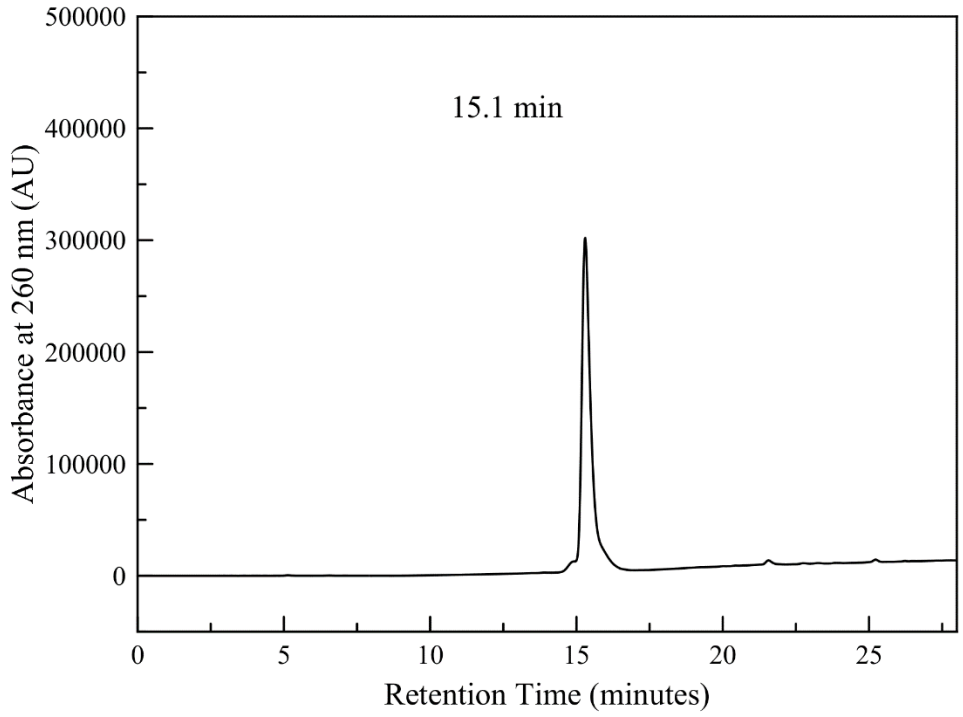

Figure S20. HPLC chromatogram of $[Co(tfacen)(NH_3)_2]^+$

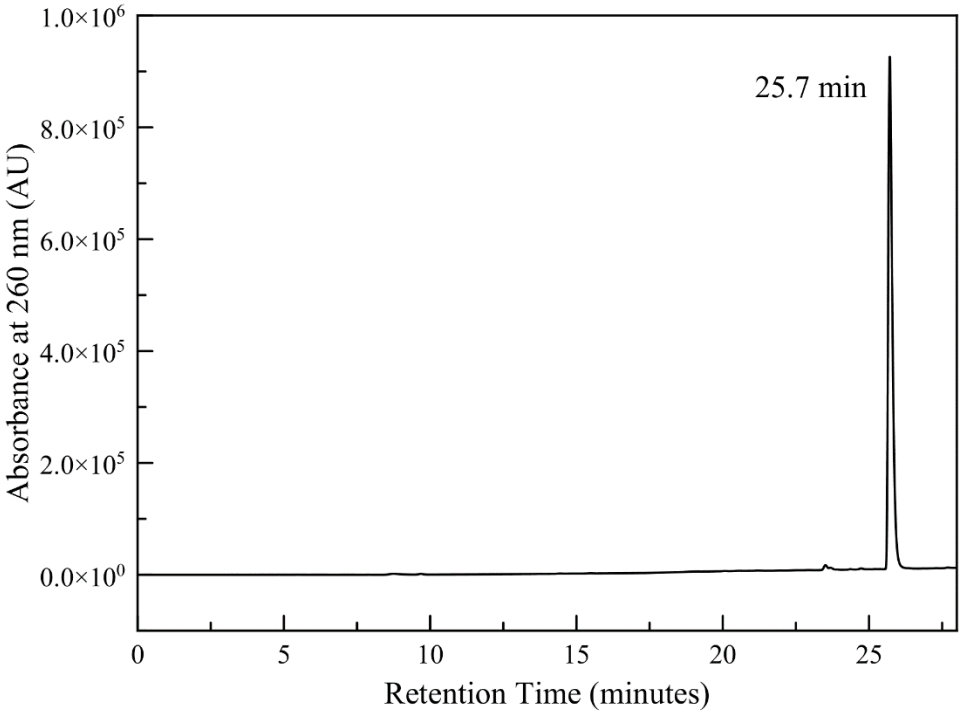

Figure S21. HPLC chromatogram of $[Co(tfacen)(3F\text{-}BnNH_2)_2]^+$

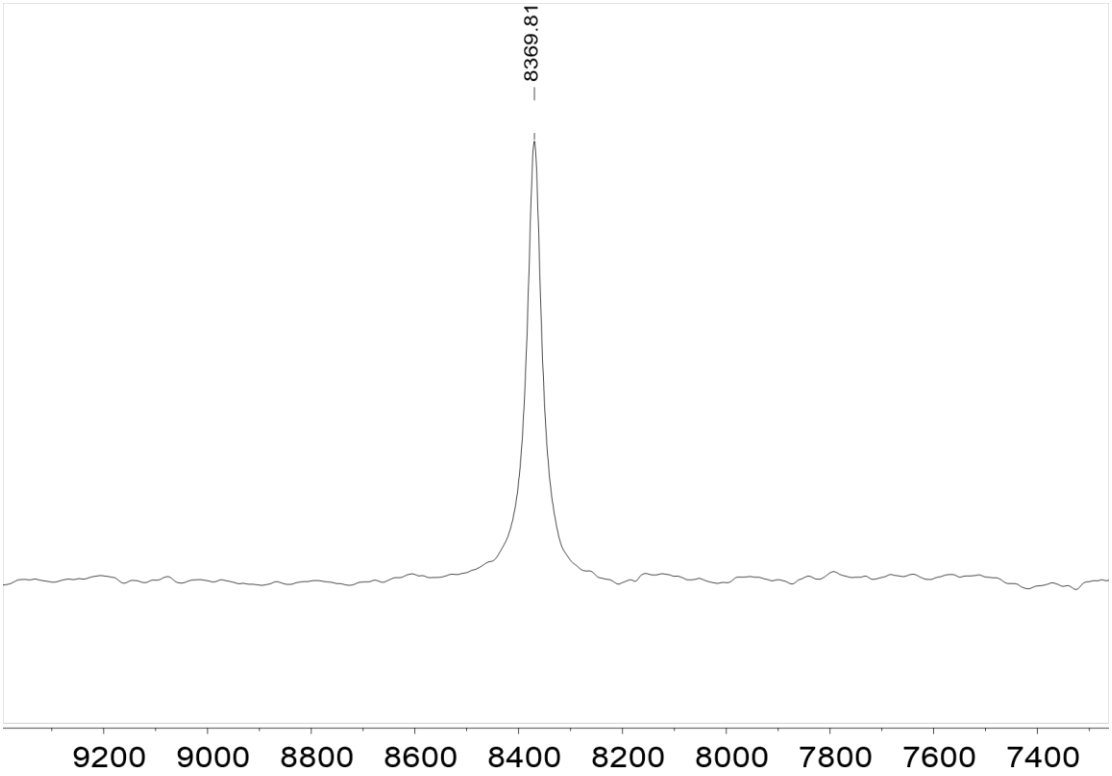

Figure S22. ^{59}Co NMR (120 MHz) spectrum of $[Co(3F\text{-}salen)(NH_3)_2]^+$ in D_2O at 298 K.

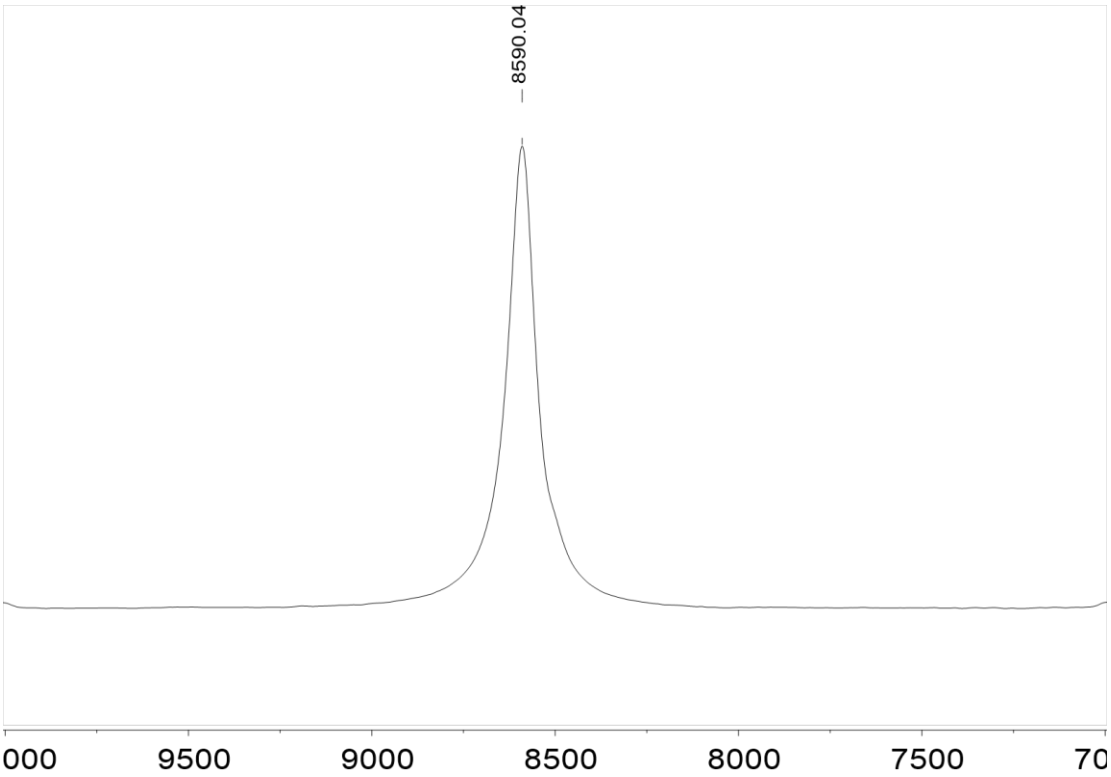

Figure S23. ^{59}Co NMR (120 MHz) spectrum of $[Co(3F\text{-}salen)(3F\text{-}BnNH_2)_2]^+$ in MeOD-d_4 at 298 K.

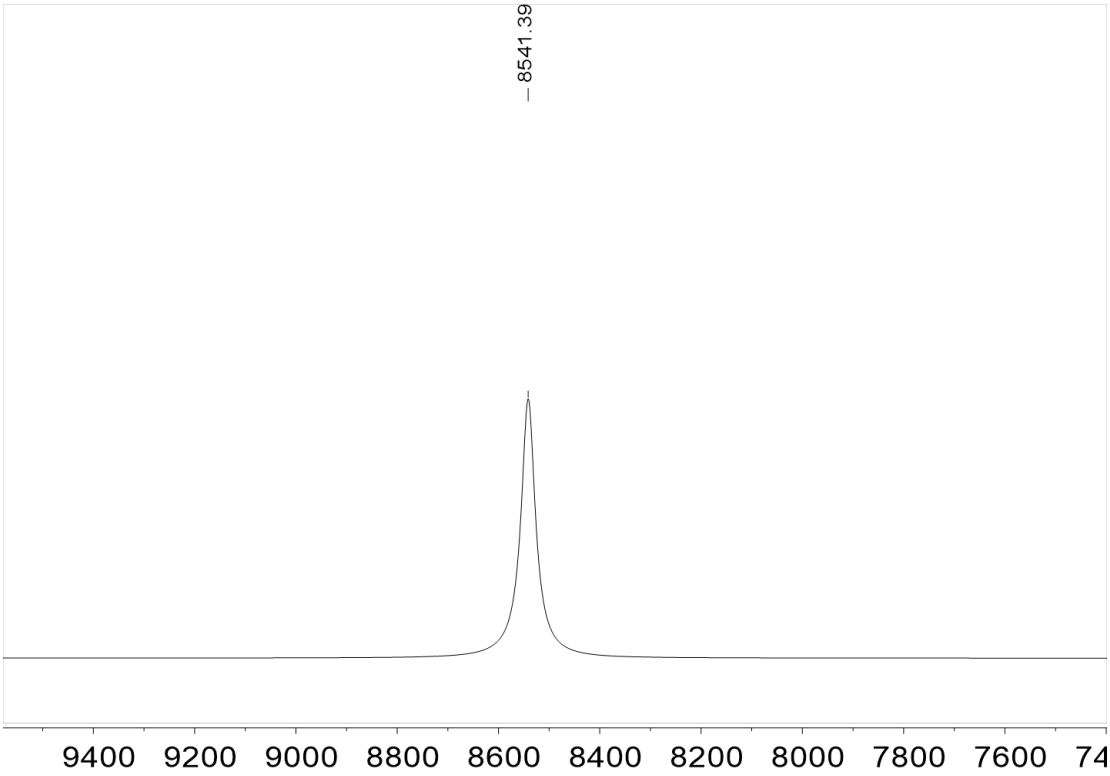

Figure S24. ^{59}Co NMR (120 MHz) spectrum of $[Co(tfacen)(NH_3)_2]^+$ in D_2O at 298 K.

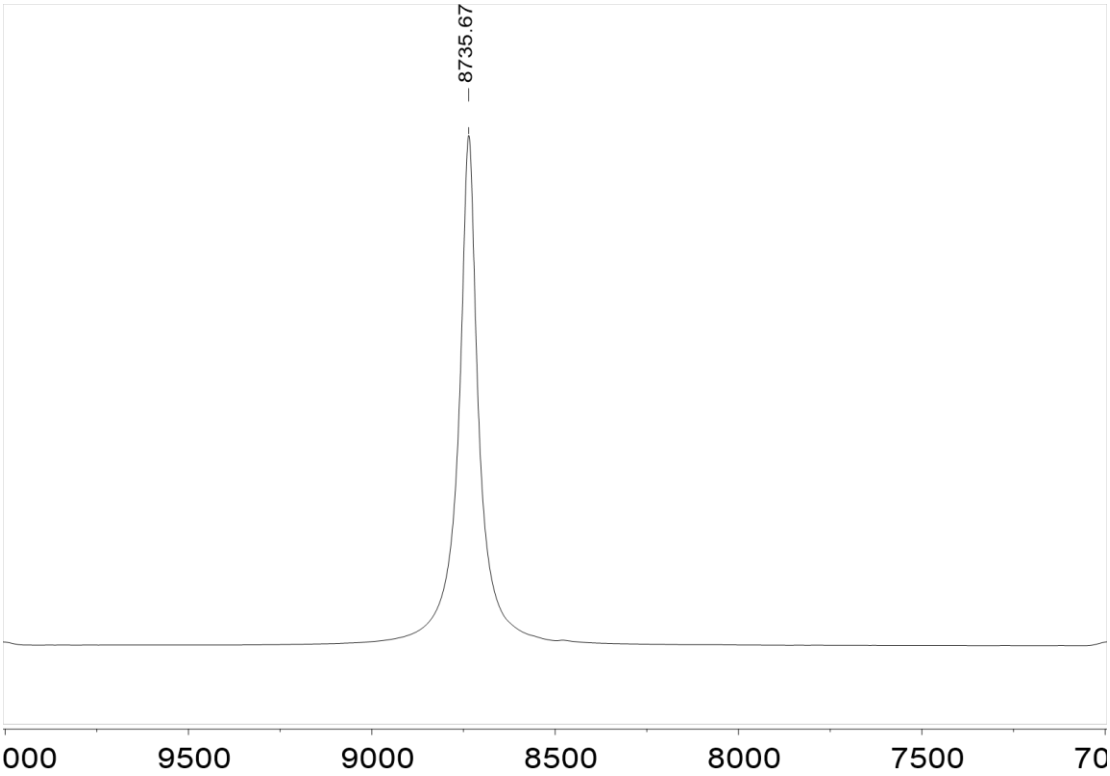

Figure S25. ^{59}Co NMR (120 MHz) spectrum of $[Co(tfacen)(3F\text{-}BnNH_2)_2]^+$ in MeOD-d_4 at 298 K.

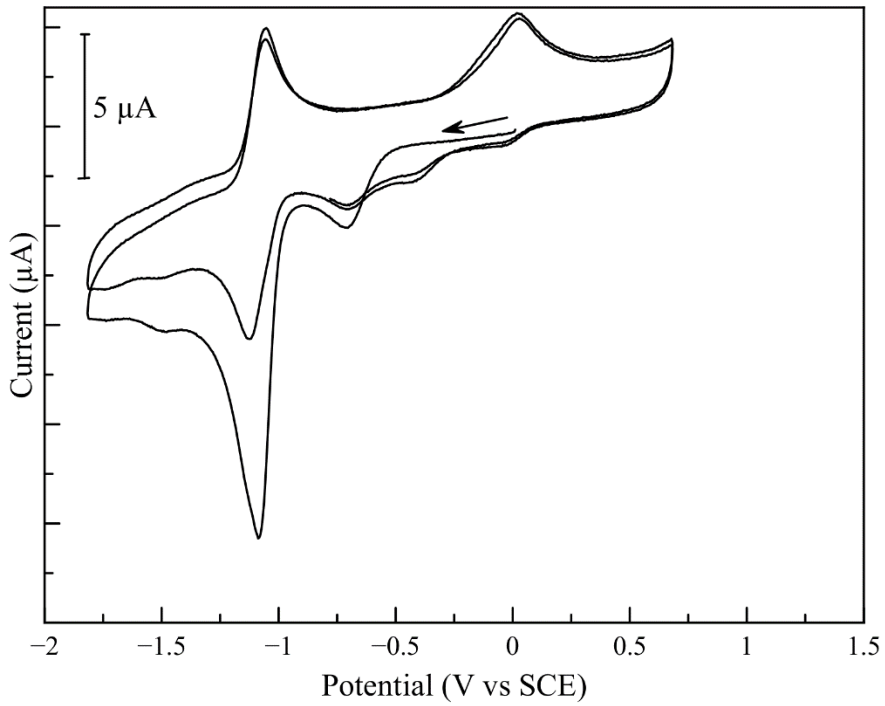

Figure S26. Cyclic voltammogram of $[Co(3F\text{-}salen)(NH_3)_2]^+$ in DMF with 0.1 M TBAP at 298 K and 0.1 V/s scan rate.

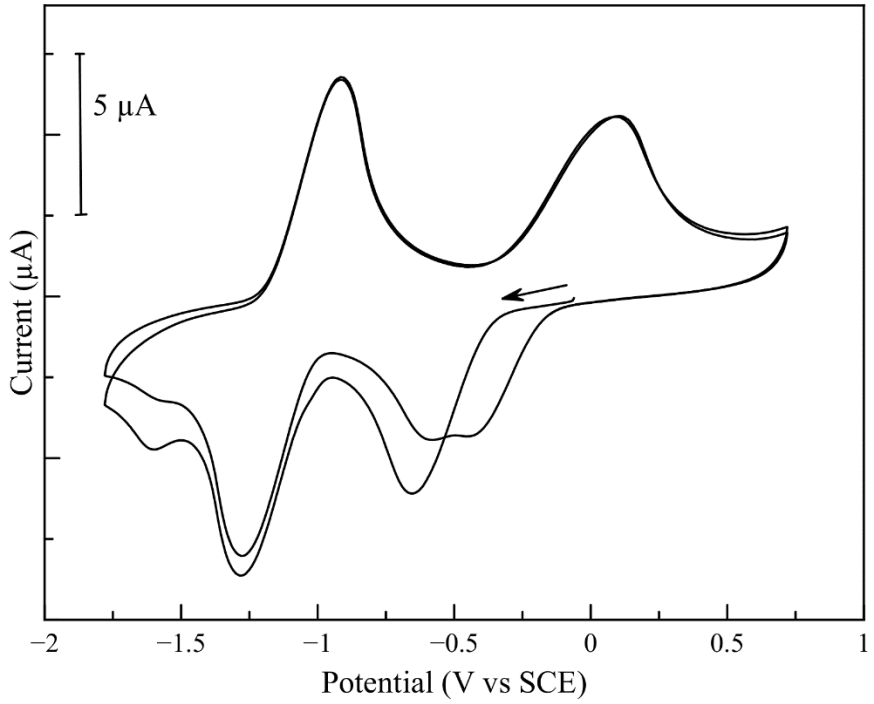

Figure S27. Cyclic voltammogram of $[Co(3F\text{-}salen)(3FBnNH_2)_2]^+$ in DMF with 0.1 M TBAP at 298 K and 0.1 V/s scan rate.

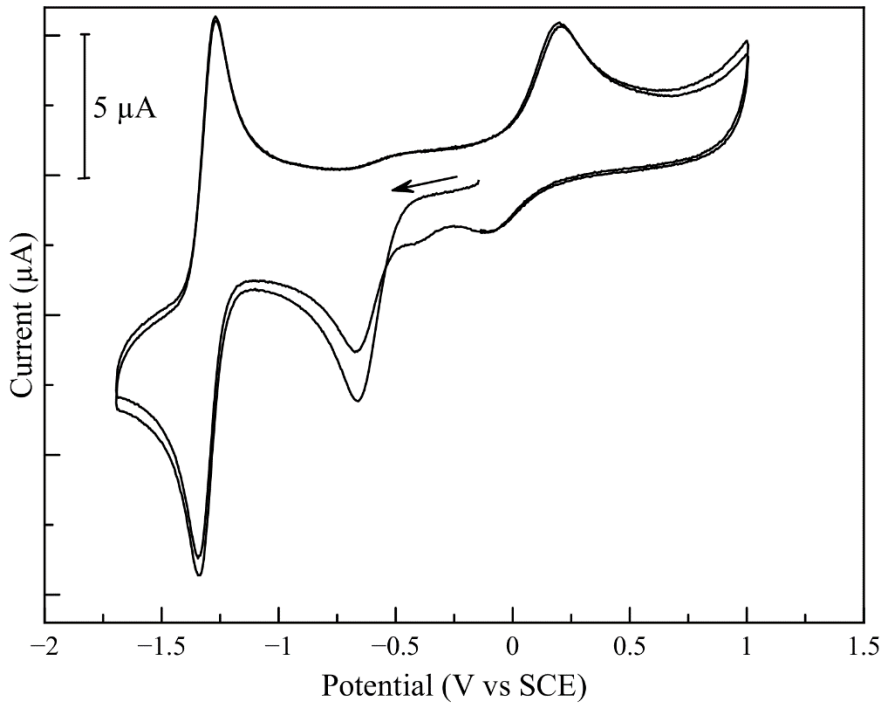

Figure S28. Cyclic voltammogram of $[Co(tfacen)(NH_3)_2]^+$ in DMF with 0.1 M TBAP at 298 K and 0.1 V/s scan rate.

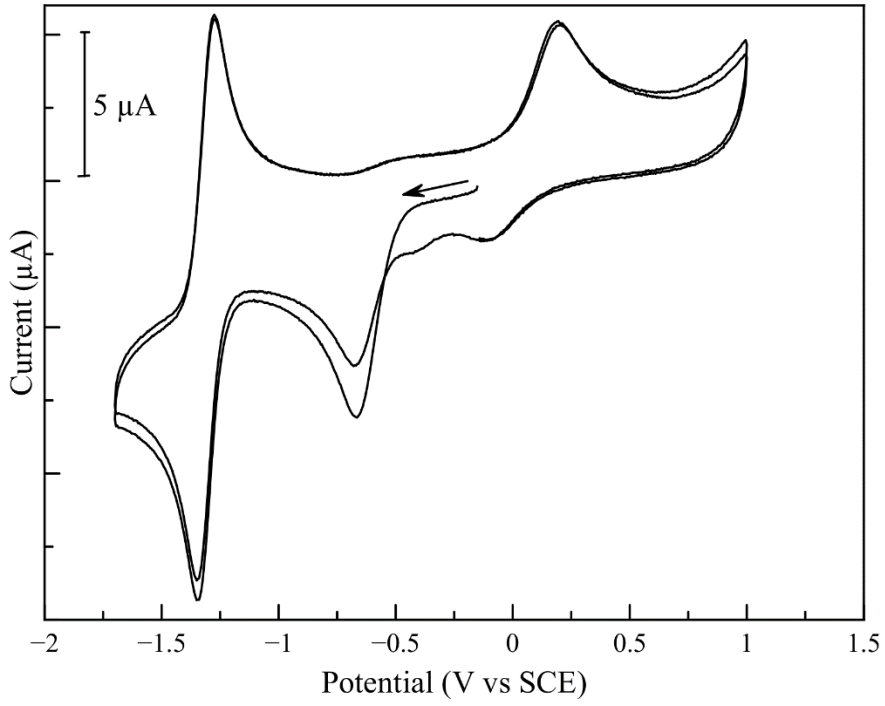

Figure S29. Cyclic voltammogram of $[Co(tfacen)(3FBnNH_2)_2]^+$ in DMF with 0.1 M TBAP at 298 K and 0.1 V/s scan rate.

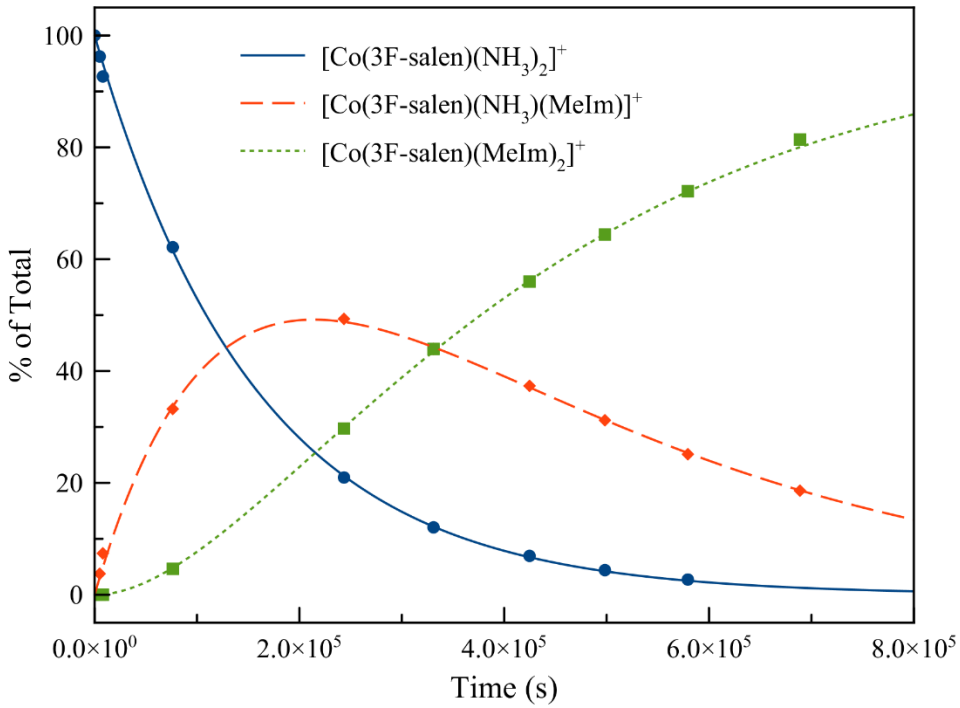

Figure S30. Concentration versus time plot for ligand exchange of $[Co(3F\text{-}salen)(NH_3)_2]^+$ by *N*-methylimidazole in 100 mM MOPS (pH 7.4) at 335 K.

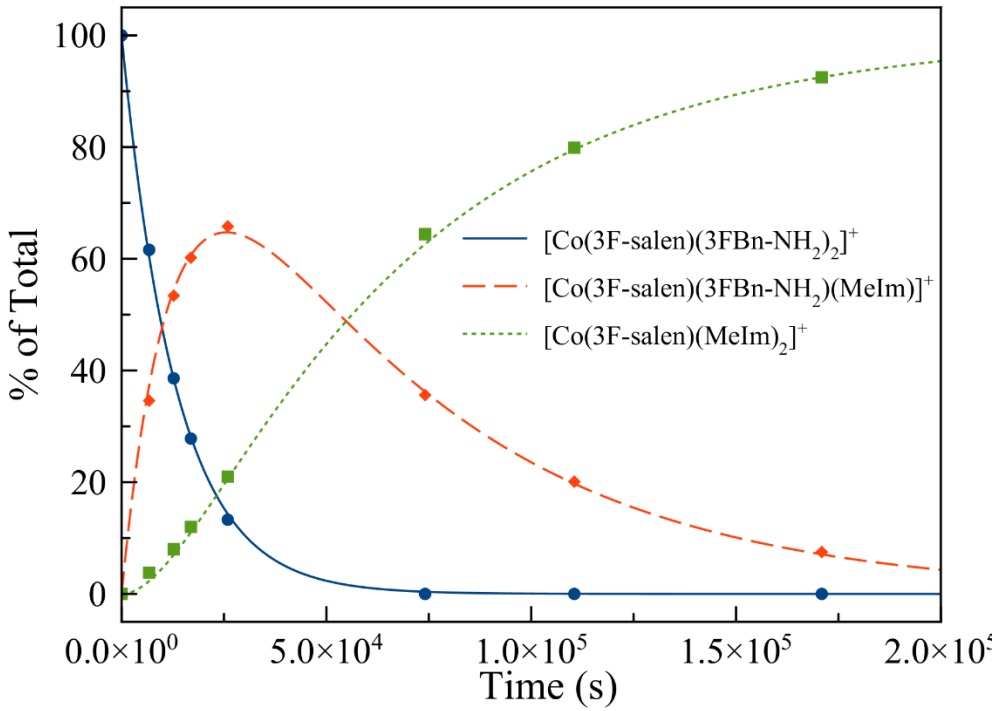

Figure S31. Concentration versus time plot for ligand exchange of $[Co(3F\text{-}salen)(3FBnNH_2)_2]^+$ by *N*-methylimidazole in 100 mM MOPS (pH 7.4) at 335 K.

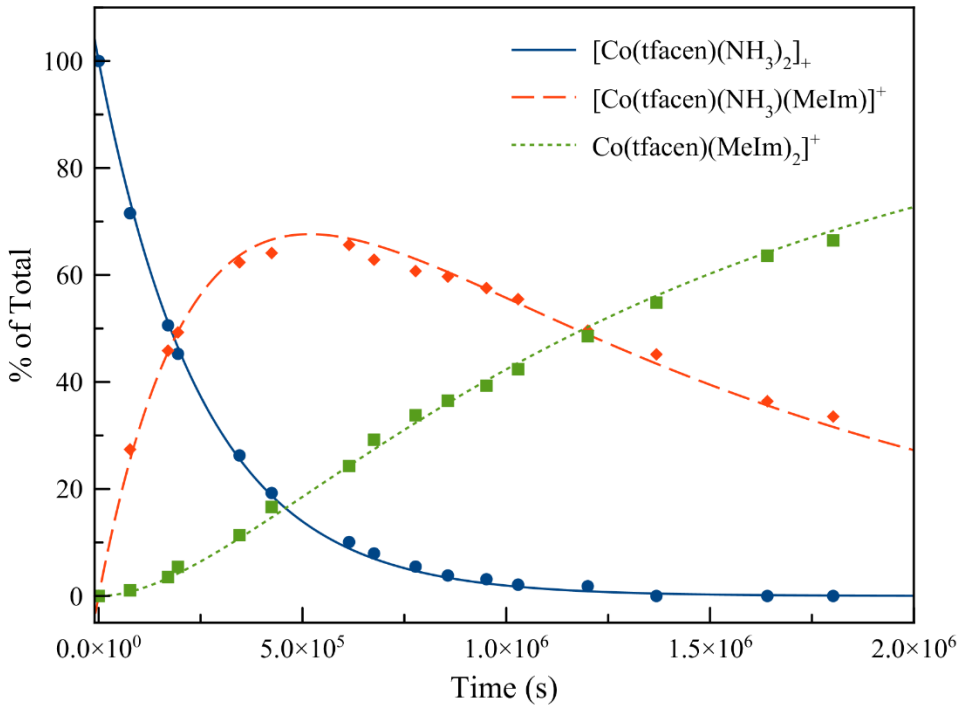

Figure S32. Concentration versus time plot for ligand exchange of $[Co(tfacen)(NH_3)_2]^+$ by *N*-methylimidazole in 100 mM MOPS (pH 7.4) at 335 K.

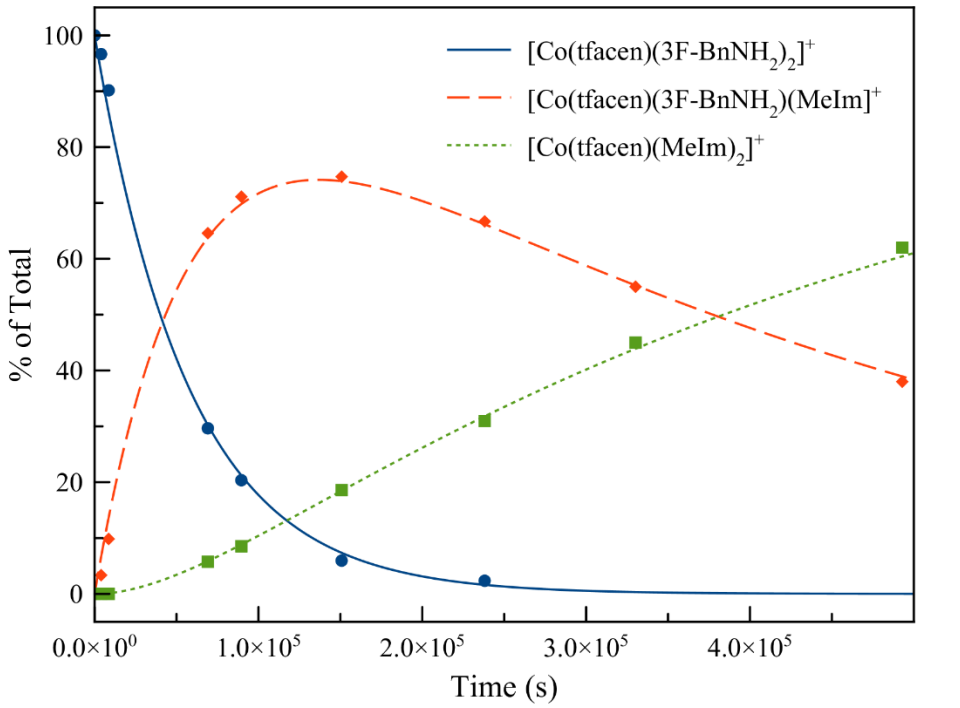

Figure S33. Concentration versus time plot for ligand exchange of $[Co(tfacen)(3FBnNH_2)_2]^+$ by *N*-methylimidazole in 100 mM MOPS (pH 7.4) at 335 K.

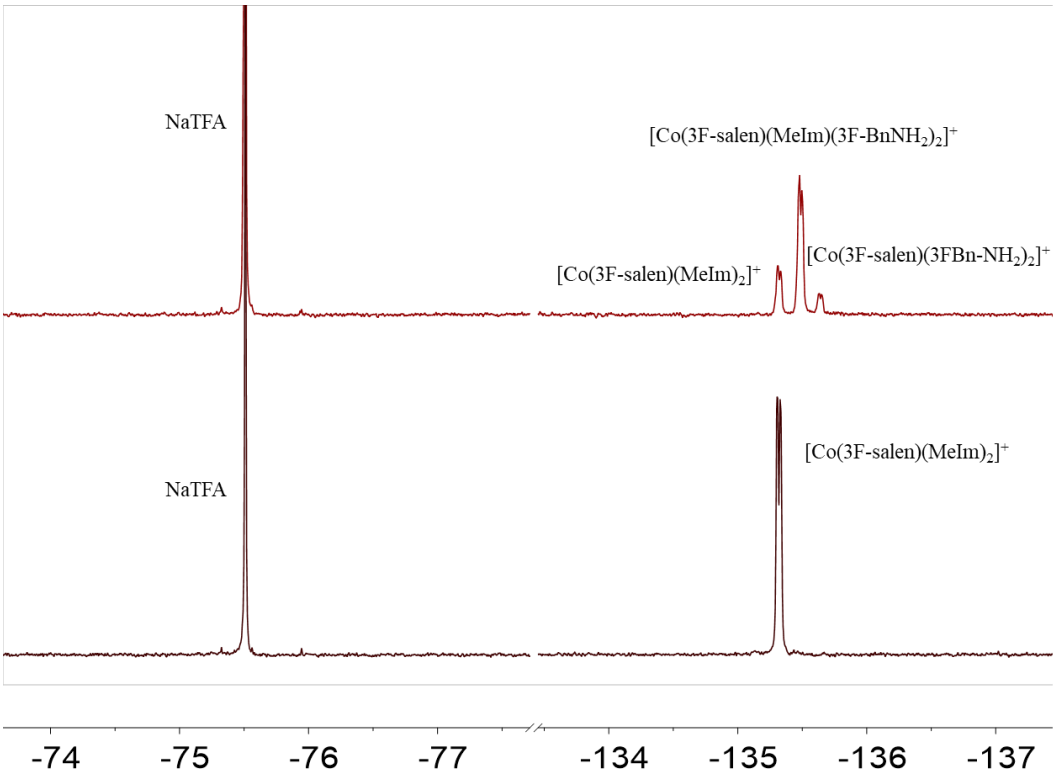

Figure S34. ^{19}F NMR (470 MHz) spectra in MOPS buffer (pH 7.4) of the ligand exchange reaction of [Co(3F-salen)(3FBnNH$_2$)$_2$]$^+$ (top trace) and a solution of [Co(3F-salen)(MeIm)$_2$]$^+$ (bottom trace). The overlay of the spectra confirms [Co(3F-salen)(MeIm)$_2$]$^+$ as the product.

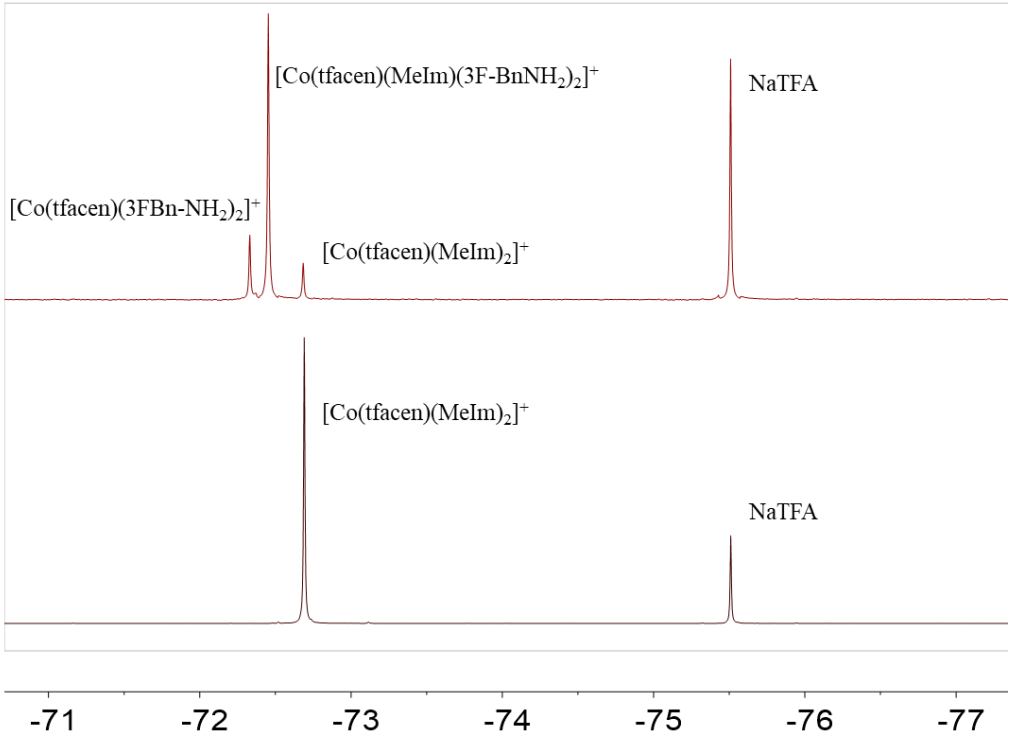

Figure S35. ^{19}F NMR (470 MHz) spectra in MOPS buffer (pH 7.4) of the ligand exchange reaction of $[Co(tfacen)(3FBnNH_2)_2]^+$ (top trace) and a solution of $[Co(tfacen)(MeIm)_2]^+$ (bottom trace). The overlay of the spectra confirms $[Co(tfacen)(MeIm)_2]^+$ as the product.

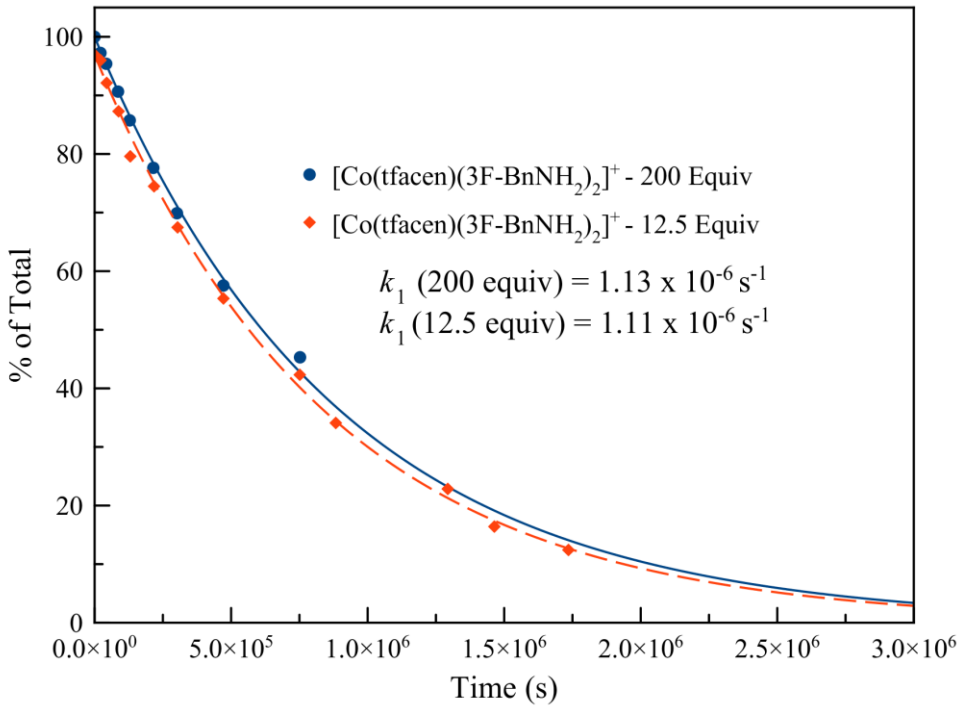

Figure S36. Concentration versus time plot for ligand exchange of $[Co(tfacen)(3F\text{-}BnNH_2)_2]^+$ by 200 equivalents of *N*-methylimidazole in 100 mM MOPS (pH 7.4) at 291 K. The calculated pseudo first-order rate constant is the same within the error for that determined with only 25 equiv of MeIm, suggesting a zero-order dependence on MeIm.

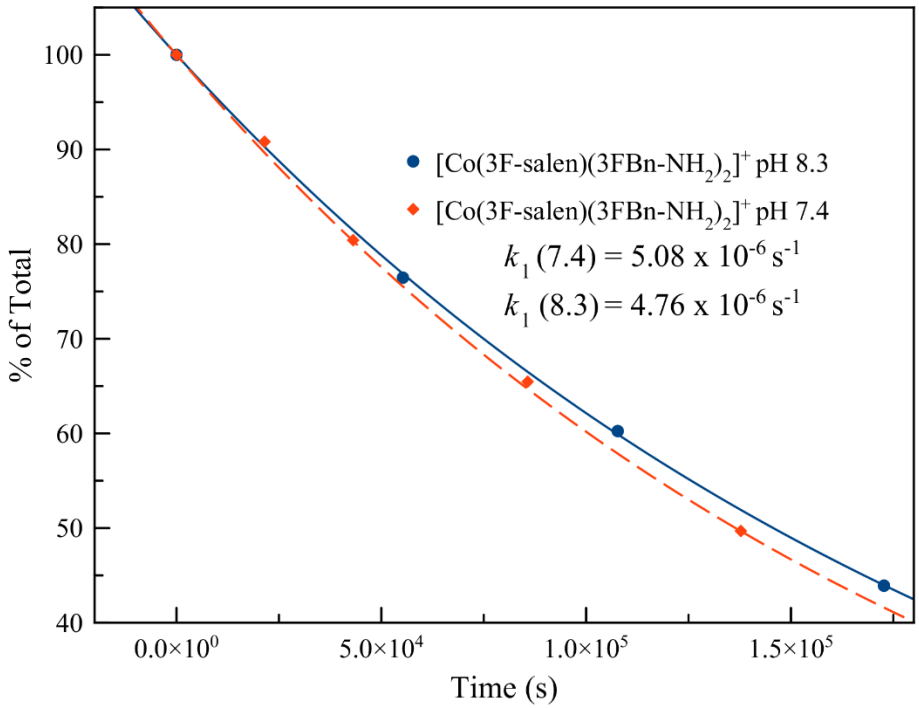

Figure S37. Concentration versus time plot for ligand exchange of $[Co(3F\text{-}salen)(3F\text{-}BnNH_2)_2]^+$ by N-methylimidazole in 100 mM MOPS (pH 8.3) at 291 K. The calculated rate constant is the same within the error for that determined at pH 7.4, suggesting that this reaction is not accelerated by this higher pH value.

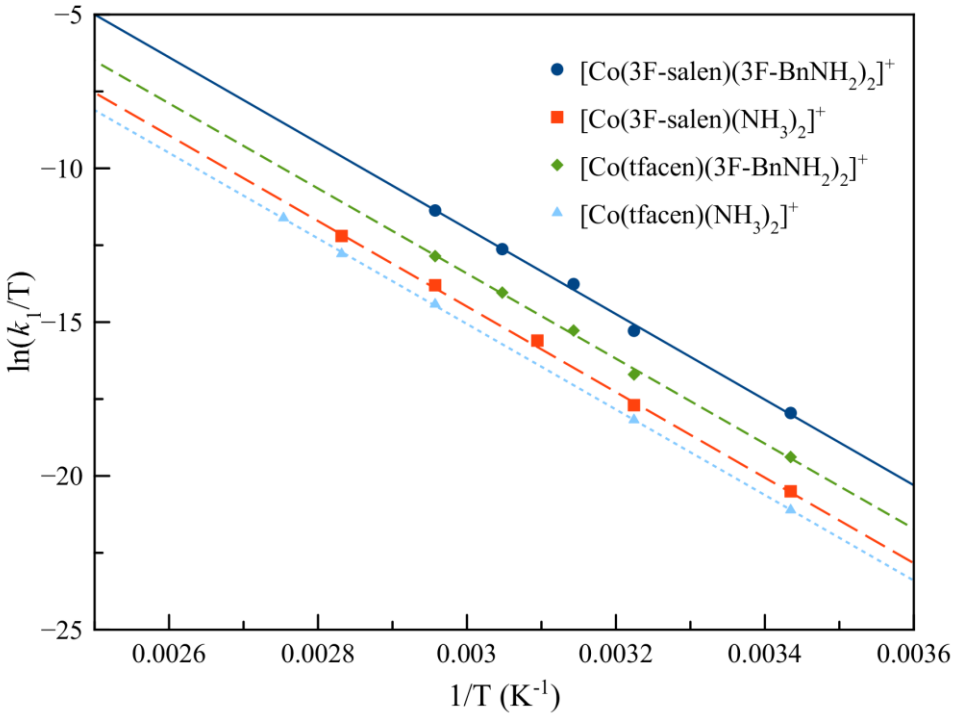

Figure S38. Eyring analysis plots demonstrating the dependence of the rate constant for the 1st ligand substitution step (k_1) on temperature.

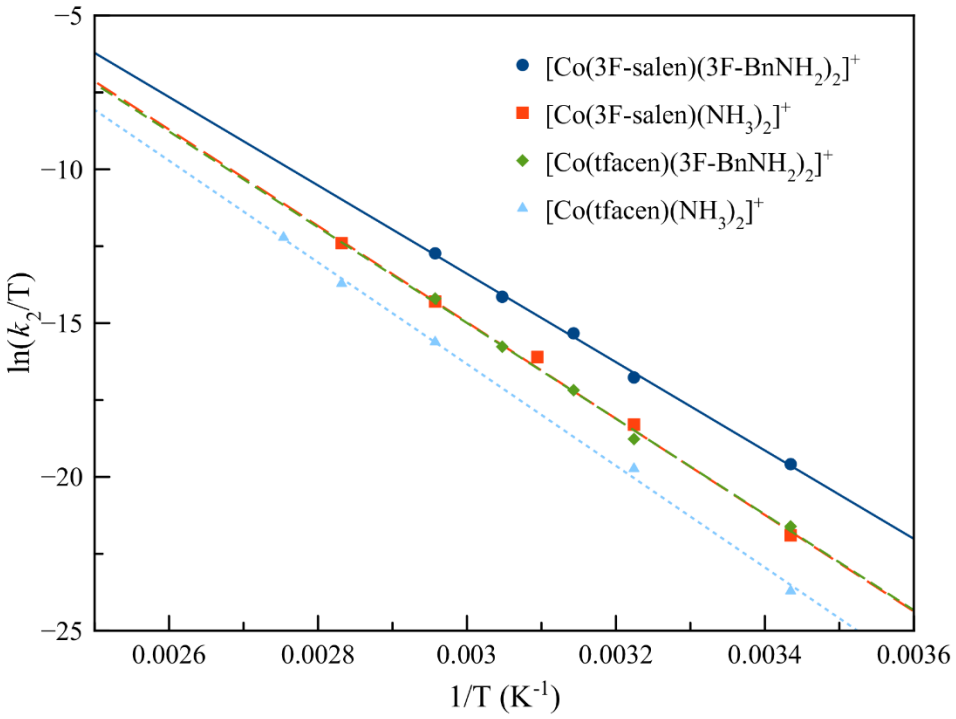

Figure S39. Eyring analysis plots demonstrating the dependence of the rate constant for the 2nd ligand substitution step (k_2) on temperature.

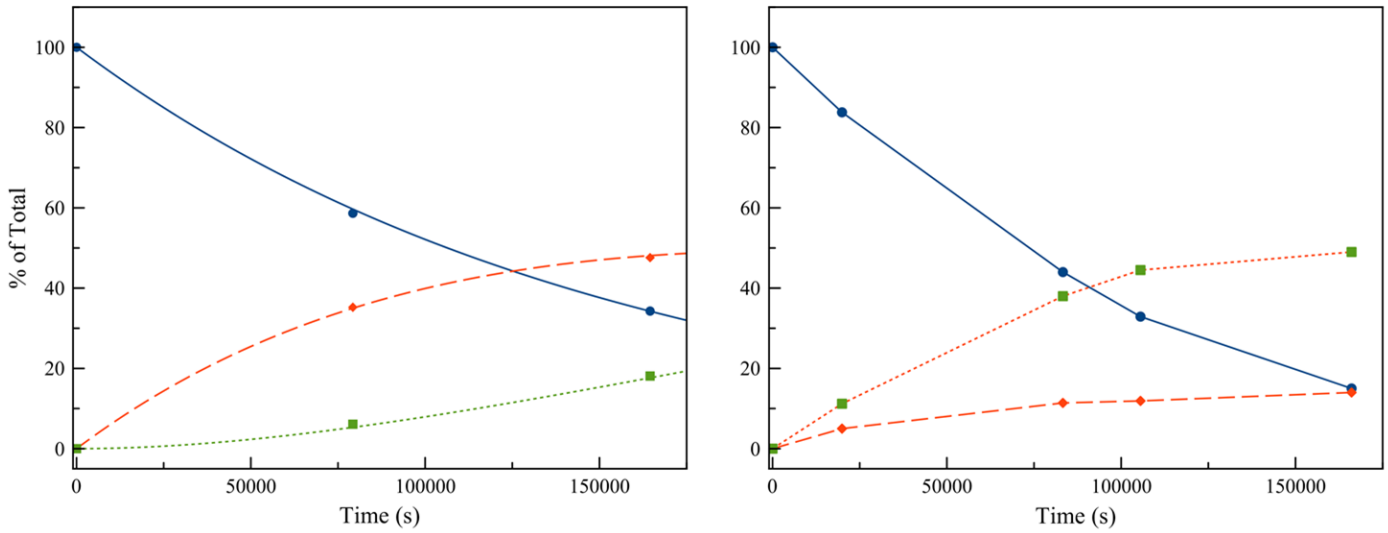

Figure S40. Representative concentration vs time data for the axial ligand substitution of [Co(3F-salen)(NH_3)$_2$]$^+$ with MeIm at 37 °C in the absence (left) and presence (right) of ascorbate. Concentrations of species (A) (circular markers), (B) (diamond markers), and (C) (square markers) refer to the starting material, monosubstituted, and disubstituted complexes, respectively.

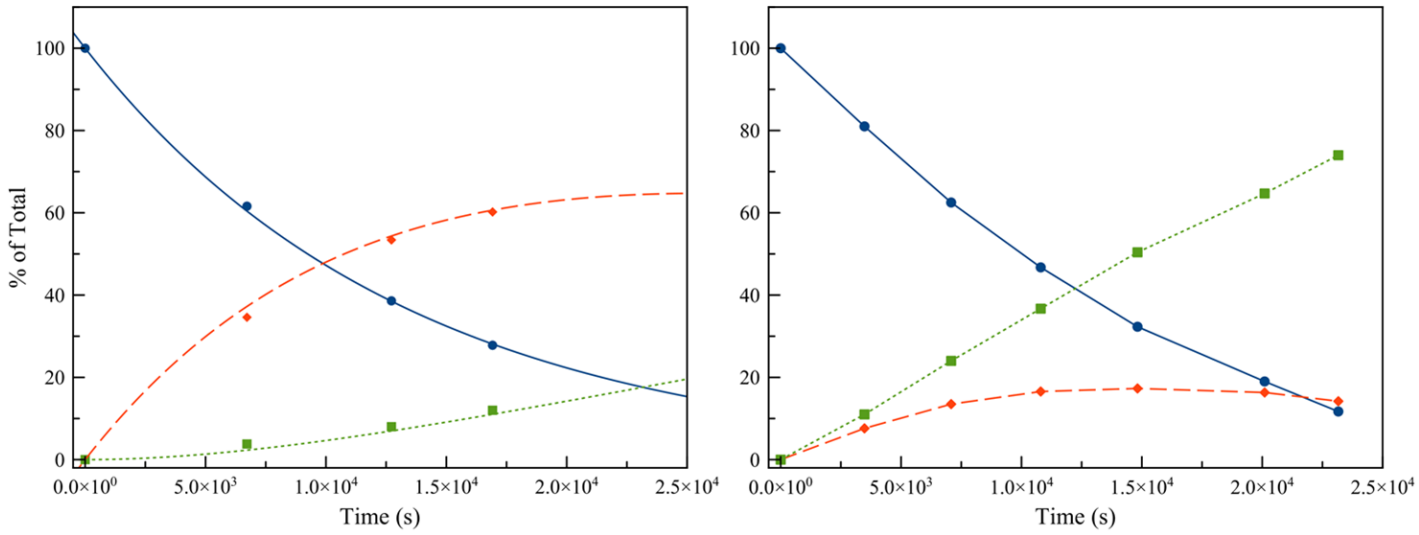

Figure S41. Representative concentration vs time data for the axial ligand substitution of $[Co(3F\text{-}salen)(3F\text{-}BnNH_2)_2]^+$ with MeIm at 37 °C in the absence (left) and presence (right) of ascorbate. Concentrations of species (A) (circular markers), (B) (diamond markers), and (C) (square markers) refer to the starting material, monosubstituted, and disubstituted complexes, respectively.

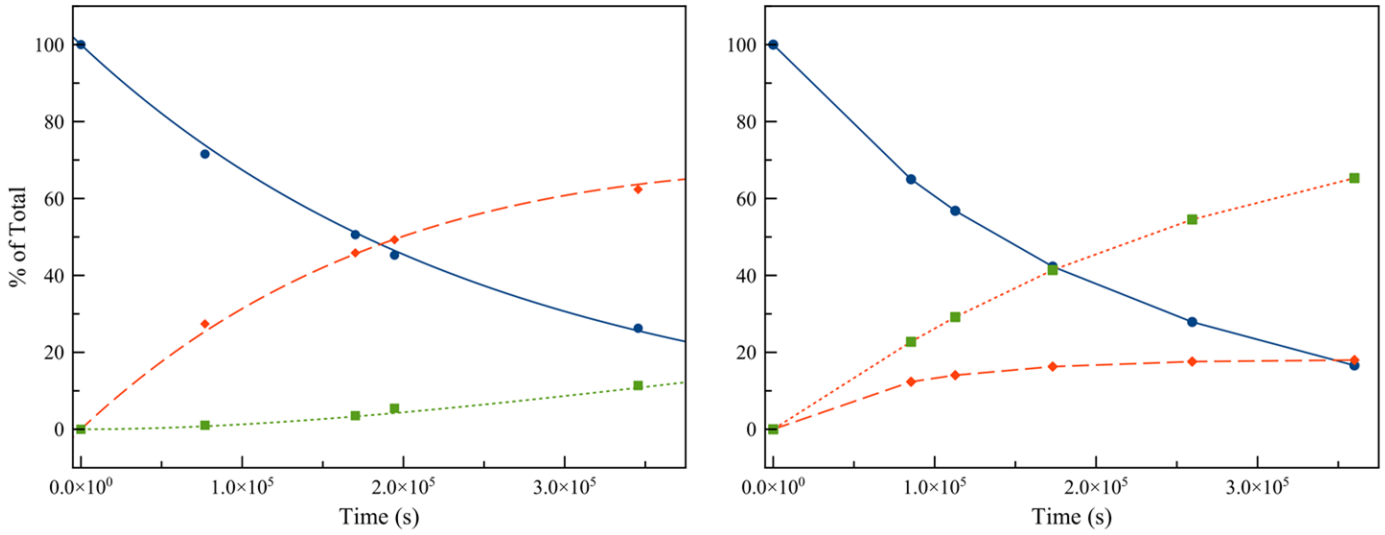

Figure S42. Representative concentration vs time data for the axial ligand substitution of $[Co(tfacen)(NH_3)_2]^+$ with MeIm at 37 °C in the absence (left) and presence (right) of ascorbate. Concentrations of species (A) (circular markers), (B) (diamond markers), and (C) (square markers) refer to the starting material, monosubstituted, and disubstituted complexes, respectively.

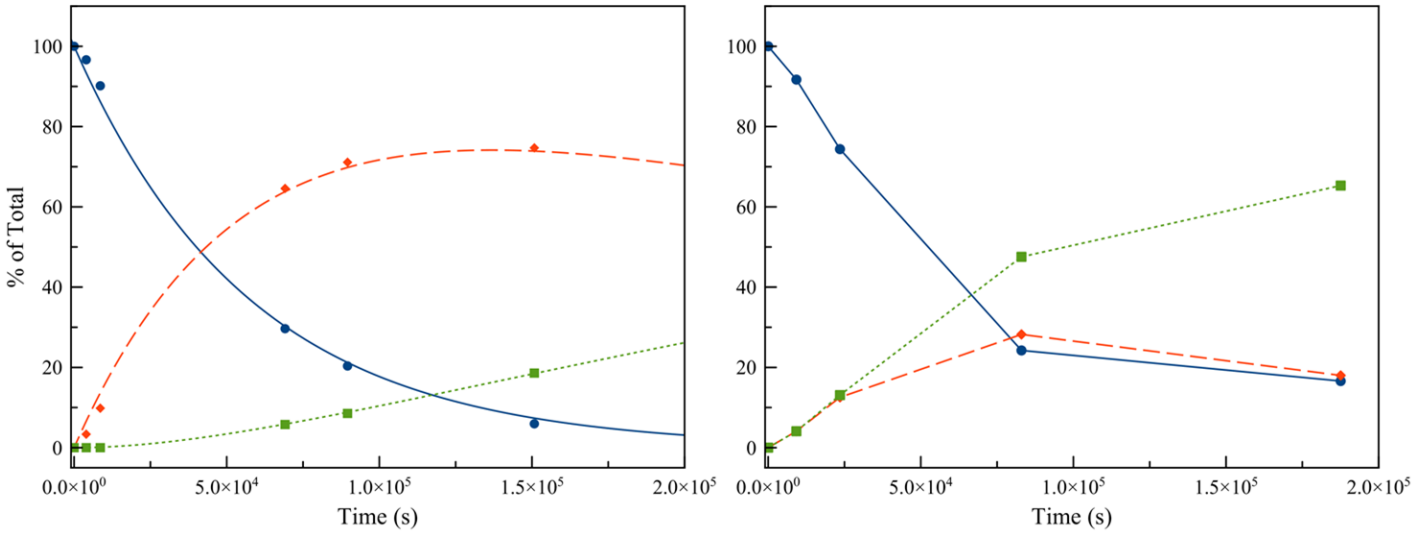

Figure S43. Representative concentration vs time data for the axial ligand substitution of $[Co(tfacen)(3F\text{-}BnNH_2)_2]^+$ with MeIm at 37 °C in the absence (left) and presence (right) of ascorbate. Concentrations of species (A) (circular markers), (B) (diamond markers), and (C) (square markers) refer to the starting material, monosubstituted, and disubstituted complexes, respectively.

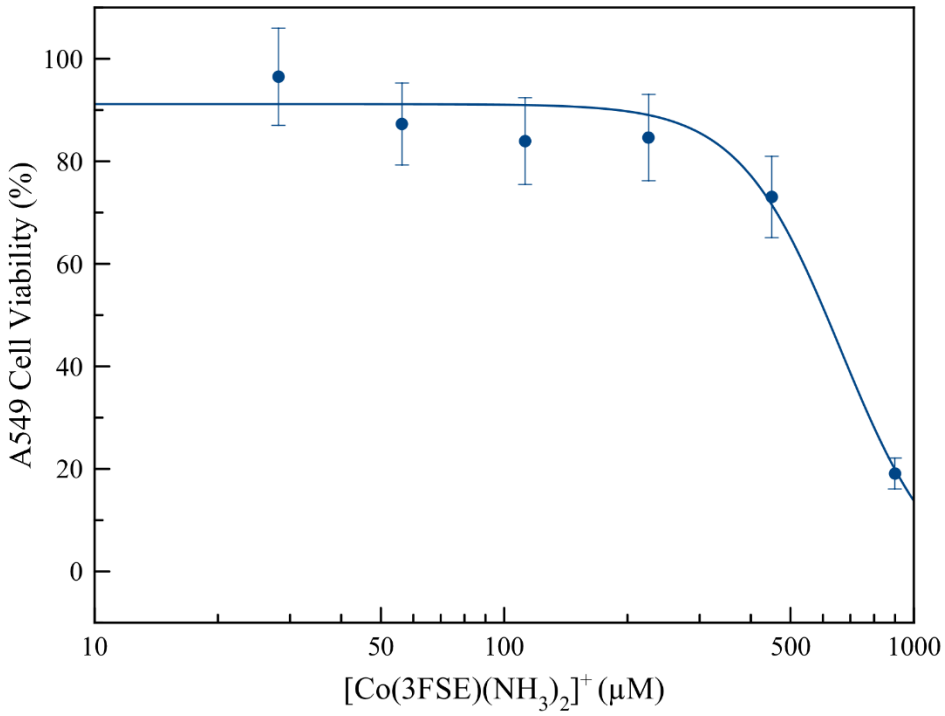

Figure S44. Dose-response curve for $[Co(3F\text{-}salen)(NH_3)_2]^+$ in A549 cells.

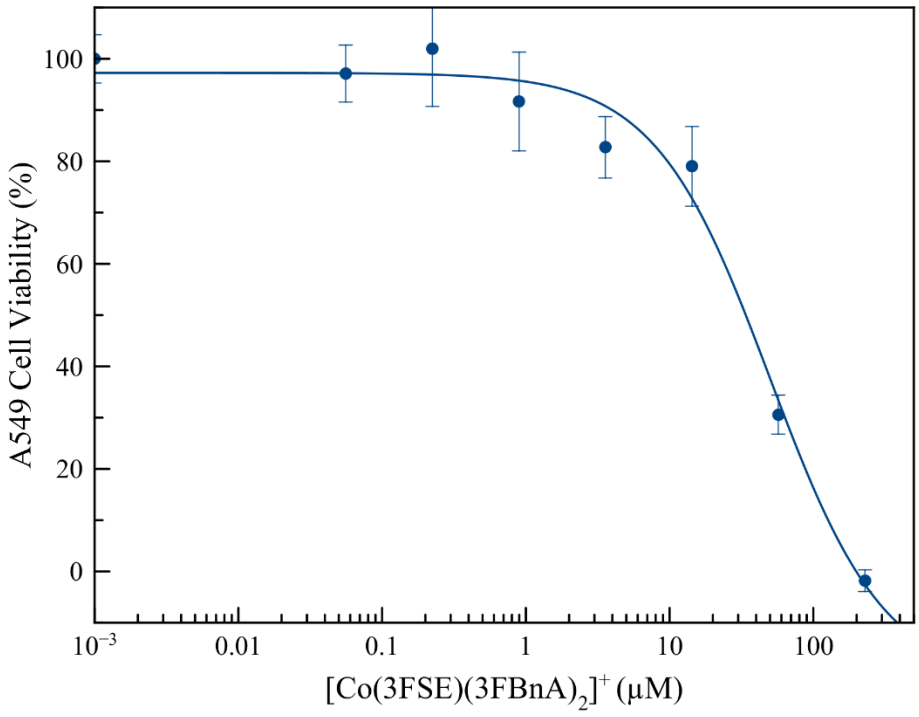

Figure S45. Dose-response curve for $[Co(3F\text{-}salen)(3F\text{-}BnNH_2)_2]^+$ in A549 cells

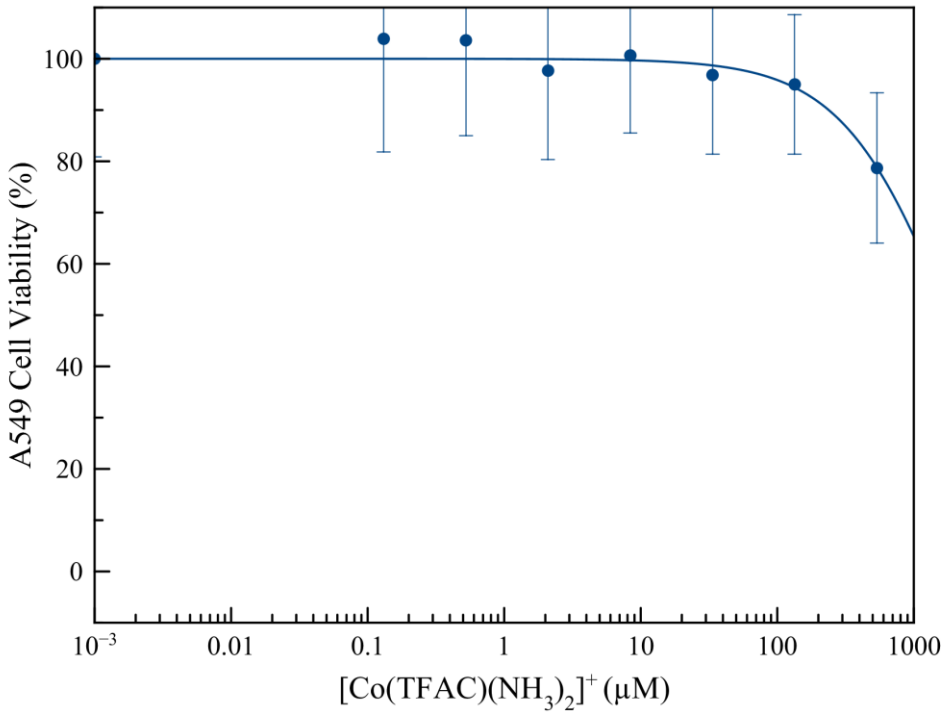

Figure S46. Dose-response curve for $[Co(tfacen)(NH_3)_2]^+$ in A549 cells

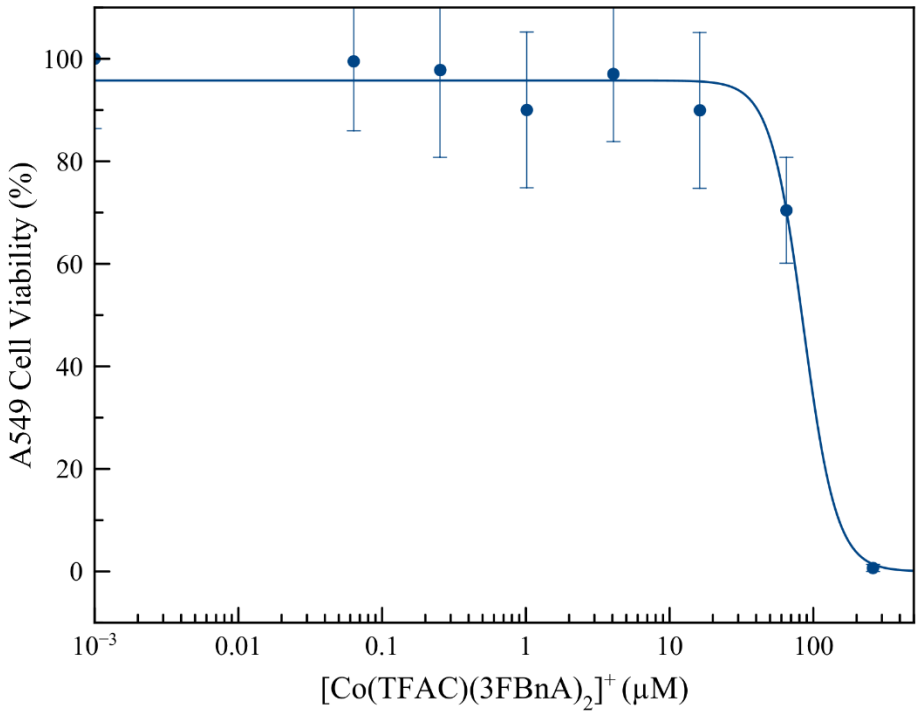

Figure S47. Dose-response curve for $[Co(tfacen)(3F\text{-}BnNH_2)_2]^+$ in A549 cells